Probing upper mantle electrical conductivity with daily magnetic variations using global-to-local transfer functions

Geophysical Journal International

Geophys. J. Int. (2019) **219,** 2125–2147
doi: 10.1093/gji/ggz412
Advance Access publication 2019 September 16
GJI Geomagnetism, Rock Magnetism and Palaeomagnetism

Probing upper mantle electrical conductivity with daily magnetic variations using global-to-local transfer functions

M. Guzavina, A. Grayver and A. Kuvshinov

Institute of Geophysics, ETH Zurich, Sonneggstrasse 5, 8092 Zurich, Switzerland. E-mail: martina.guzavina@erdw.ethz.ch

Accepted 2019 September 12. Received 2019 August 29; in original form 2019 February 26

SUMMARY

We present new transfer functions (TFs) that can handle external electromagnetic (EM) sources of complex geometry. These TFs relate global expansion coefficients describing the source with a locally measured EM field. In this study, the new TFs concept was applied to the daily magnetic variations measured at the ground. The parametrization of the source in terms of spherical harmonics was adopted. We used nearly 20 yr of data from 125 mid-latitude observatories and explored how the results are affected by (i) solar activity conditions, (ii) the choice of the prior conductivity model used for the source coefficient estimation and (iii) the presence of ocean tidal magnetic signals. We found that choosing magnetically quiet periods is beneficial due to simpler source morphology, and the choice of prior conductivity model may significantly affect the source coefficients and TFs at short periods. We further observed significant contributions by ocean tidal magnetic signals at coastal and island observatories and corrected for them. Finally, the estimated TFs were inverted for the mantle conductivity at several locations representing different geological settings.

Key words: Composition and structure of the mantle; Electromagnetic theory; Geomagnetic induction; Spatial analysis; Time-series analysis.

1 INTRODUCTION

Electrical conductivity is sensitive to water content, as well as to chemical composition, temperature and melt (e.g. Yoshino 2010; Karato & Wang 2013). However, the recovery of conductivity in the mantle is a non-trivial task, in particular due to uneven and sparse distribution of magnetic observatories across the globe, which are the main source of data for such a recovery. Nevertheless, a few 3-D semi-global (Fukao *et al.* 2004; Koyama *et al.* 2006, 2014; Utada *et al.* 2009; Shimizu *et al.* 2010) and global (Kelbert *et al.* 2009; Tarits & Mandea 2010; Semenov & Kuvshinov 2012; Sun *et al.* 2015) mantle conductivity models were published. These models are based on the analysis of the ground-based geomagnetic field variations with periods longer than 1 d. These variations mostly originate from the magnetospheric ring current, which is usually described by a single zonal spherical harmonic (SH) $Y_1^0 = \cos\vartheta$. In this case, the electrical conductivity can be obtained by inverting the so-called local C-responses (Banks 1969), that relate locally measured vertical and tangential magnetic field variations. Due to their frequency content, these data have limited sensitivity in the upper mantle (e.g. Kelbert *et al.* 2008; Püthe *et al.* 2015a; Grayver *et al.* 2017).

Tighter constrains on the electrical structure in the upper mantle and the mantle transition zone (MTZ) would require considering geomagnetic field variations in a period range between a few hours and 1 d. The dominating source of these variations is ionospheric current systems (e.g. Yamazaki & Maute 2017), which have much more complex spatio-temporal structure than the magnetospheric ring current. Despite this, there were a number of studies that analysed daily magnetic variations and utilized a variant of local C-response concept which represents the source by using a single SH (Schmucker 1970; Bahr & Filloux 1989; Simpson *et al.* 2000; Simpson 2002). However, presently there exists a consensus that the description of the ionospheric source by a single SH is too simplistic. Alternatively, local C-responses can be estimated without prior assumptions about the source geometry (Schmucker 1984; Olsen 1992, 1998). Such estimation requires local tangential gradients of the tangential magnetic field. Since direct measurement of the gradients is extremely challenging in practice, they are commonly computed with the use of tangential magnetic field measured at an array of observation sites located nearby. The prerequisite for successful implementation of this approach is a relatively dense regional grid of observations in the region of interest. This significantly limits its wide practical adoption.

To overcome the discussed difficulties, Koch & Kuvshinov (2013) explored the approach proposed by Fainberg *et al.* (1990) for analysing daily magnetic variations. Rather than working with the C-responses, they work with field spectra directly. Despite promising results (Koch & Kuvshinov 2015), the analysis of spectra has one significant shortcoming: it requires an actual description of the source. In practice, however, one determines the source with an inevitable error, and this injects an undesired and uncontrolled uncertainty into the recovered conductivity models.

To overcome the problem, Püthe *et al.* (2015b) introduced an alternative concept which is also capable of handling sources of arbitrary complexity. It was originally designed to account for the non-zonal contributions to the magnetospheric ring current, and is based on a new type of transfer functions (TFs) that relate expansion coefficients describing the source globally with a locally measured electromagnetic (EM) field, hence we refer to them as global-to-local TFs. With the new responses, one avoids complications of finding the actual description of the source. The approach only requires to specify a set of basis functions (in our case SH) which describe the source geometry reasonably well. Additionally, this approach enables us to estimate statistical uncertainties of the TFs.

In this paper, we discuss applicability of this approach to the daily magnetic variations and invert estimated TFs at multiple locations for mantle conductivity.

2 METHODOLOGY

2.1 Introducing TFs

Daily magnetic variations have predominantly ionospheric origin, with some contribution, however, from magnetosphere. Atmospheric tides are the driving force of ionospheric solar quiet (Sq) and lunar (L) variations. Specifically, Sq variations are driven by tides excited through thermal heating from Sun. In contrast, L variations are driven by tides due to the lunar gravitational pull (Lindzen & Chapman 1969; Olsen 1991). Diurnal variations of the magnetospheric origin result, for instance, from magneto-tail currents (Lühr *et al.* 2017).

Time-varying magnetic variations are governed by Maxwell's equations. In frequency-domain, Maxwell's equations (with time dependency expressed as $e^{\mathrm{i}\omega t}$) are given by

$$\begin{aligned} \frac{1}{\mu_0}\nabla\times\vec{B} &= \sigma\vec{E}+\vec{j}^{\,\mathrm{ext}} \\ \nabla\times\vec{E} &= -\mathrm{i}\omega\vec{B}, \end{aligned} \tag{1}$$

where $\vec{j}^{\,\mathrm{ext}}(\vec{r},\omega)$ is an extraneous electric current, $\vec{B}(\vec{r},\omega)$ and $\vec{E}(\vec{r},\omega)$ magnetic and electric fields, respectively, μ_0 magnetic permeability of free space, $\sigma(\vec{r})$ spatial distribution of electrical conductivity and ω angular frequency. The position vector $\vec{r}=(r,\vartheta,\varphi)$ describes a spherical coordinate system, with r, ϑ and φ being distance from the Earth's centre, colatitude and longitude, respectively.

We assume that the region with extraneous (source) electric currents is surrounded by an insulator (such as air), therefore it becomes possible to collapse it into an infinitely thin spherical sheet at an altitude h. This allows us to represent this current using a current function, Ψ, as

$$\vec{j}^{\,\mathrm{ext}}(\vec{r},\omega) = -\delta(r-b)\,\vec{E}_r\times\nabla_H\Psi(\Omega,\omega), \tag{2}$$

where δ is Dirac's delta function, $\Omega=(\vartheta,\varphi)$, $b=a+h$ where $a=6371.2$ km Earth's mean radius, ∇_H tangential gradient and $\vec{E}_r$ radial unit vector of the spherical coordinate system.

In what follows, we will consider the diurnal period and its harmonics, thus $\omega_p=\frac{2\pi p}{T}$, where $p=1,2,\ldots$ and $T=24$ hr. In practice, we found time harmonics with $p>6$ (corresponding to variations with periods shorter than 4 hr) contribute insignificantly to the total signal and will not be considered further.

We will assume further that Ψ is a linear combination of spatial modes, leading to

$$\Psi(\Omega,\omega_p) = \sum_{l\in L(p)}\varepsilon_l(\omega_p)\Psi_l(\Omega), \tag{3}$$

where $L(p)$ denotes a set of modes which describes the source at a frequency ω_p; the specific form of spatial modes used in this study will be given later. Using eqs (2) and (3), one can write $\vec{j}^{\,\mathrm{ext}}$ as

$$\vec{j}^{\,\mathrm{ext}}(\vec{r},\omega_p) = \sum_{l\in L(p)}\varepsilon_l(\omega_p)\,\vec{j}_l(\vec{r}), \tag{4}$$

where

$$\vec{j}_l(\vec{r}) = -\delta(r-b)\,\vec{E}_r\times\nabla_H\Psi_l(\Omega). \tag{5}$$

By considering Maxwell's equations for each $\vec{j}_l$

$$\begin{aligned} \frac{1}{\mu_0}\nabla\times\vec{B}_l &= \sigma\vec{E}_l+\vec{j}_l \\ \nabla\times\vec{E}_l &= -\mathrm{i}\omega_p\vec{B}_l, \end{aligned} \tag{6}$$

and exploiting the linearity of Maxwell's equations with respect to the source, one can represent the magnetic field at the observation site, $\vec{r}_{\mathrm{o}}$, as a sum

$$\vec{B}(\vec{r}_{\mathrm{o}},\omega_p) = \sum_{l\in L(p)}\varepsilon_l(\omega_p)\,\vec{B}_l(\vec{r}_{\mathrm{o}},\omega_p). \tag{7}$$

$\vec{B}_l(\vec{r}_{\mathrm{o}},\omega_p)$ represent global-to-local arrays of 'magnetic field' TFs relating 'global' source coefficients ε_l to 'local' components of magnetic field at the observation site $\vec{r}_{\mathrm{o}}$.

New TFs provide a lot of flexibility. First of all, they are local and thus suitable for working with sparse and irregularly distributed ground-based data. Furthermore, eq. (7) holds both above and inside the Earth. Therefore, derived TFs can also be estimated for stations at the sea bottom. Finally, in addition to the 'magnetic field' TFs, one can exploit tangential electric field measurements (either ground-based or/and sea-bottom), and estimate 'electric field' TFs, $\vec{E}_{\tau,l}(\vec{r}_{\mathrm{o}},\omega_p)$, as

$$\vec{E}_\tau(\vec{r}_{\mathrm{o}},\omega_p) = \sum_{l\in L(p)}\varepsilon_l(\omega_p)\,\vec{E}_{\tau,l}(\vec{r}_{\mathrm{o}},\omega_p). \tag{8}$$

Here, subscript τ denotes tangential component. Note, however, that analysis of ground-based electric field measurements is challenging due to the presence of galvanic distortions (Jiracek 1990).

So far, we have not chosen spatial modes for approximating geometry of the source current. In this study, we will work with SH functions. Specifically, current function Ψ is parametrized as (Schmucker 1984, pp. 70–71)

$$\Psi(\vec{r},\omega_p) = -\frac{a}{\mu_0}\sum_{n,m\in L(p)}\frac{2n+1}{n+1}\left(\frac{b}{a}\right)^n\epsilon_n^m(\omega_p)S_n^m(\vartheta,\varphi). \tag{9}$$

It allows us to write the source $\vec{j}^{\,\mathrm{ext}}$ as

$$\vec{j}^{\,\mathrm{ext}}(\vec{r},\omega_p) = \sum_{n,m\in L(p)}\varepsilon_n^m(\omega_p)\,\vec{j}_n^{\,m}(\vec{r}), \tag{10}$$

where $\vec{j}_n^{\,m}$ has a form

$$\vec{j}_n^{\,m}(\vec{r}) = \frac{\delta(r-b)}{\mu_0}\frac{2n+1}{n+1}\left(\frac{b}{a}\right)^{n-1}\vec{E}_r\times\nabla_\perp S_n^m. \tag{11}$$

Here $\nabla_\perp=r\nabla_H$, and n and m are, respectively, degree and order of the spherical harmonic $S_n^m=P_n^{|m|}(\cos\vartheta)e^{\mathrm{i}m\varphi}$ with $P_n^{|m|}$ given by the Schmidt quasi-normalized associated Legendre functions. Note that the current in eqs (10) and (11) flowing in a shell $r = b > a$ embedded in an insulator will produce exactly the external magnetic field $\vec{B}^{\text{ext}}$ below the shell in the region $a \leq r < b$ [*cf.* appendix G of Kuvshinov & Semenov (2012)]. Representation of the magnetic field (above the Earth's surface) via external and internal parts is further elaborated in Appendix A.

Following Schmucker (1999), double sum in eq. (9) is given by

$$\sum_{n,m \in L(p)} = \sum_{m=p-1}^{p+1} \sum_{n=m}^{m+3}. \tag{12}$$

Table 1 lists combinations of (n, m) for each p, and bold entries highlight the expected dominant terms for each p. The choice of (n, m) combinations is discussed in more detail in Appendix B. This parametrization is suitable for describing Sq variations (Schmucker 1999), but may be suboptimal for lunar variations and variations of magnetospheric origin. However, by assuming that Sq variations are the dominant signal, this parametrization seems justified. We note that the presented formalism allows one to easily adopt alternative parametrizations.

With the introduced parametrization, eqs (6) and (7) can be rewritten as

$$\begin{aligned} \frac{1}{\mu_0} \nabla \times \vec{B}_n^m &= \sigma \vec{E}_n^m + \vec{j}_n^m \\ \nabla \times \vec{E}_n^m &= -\mathrm{i}\omega_p \vec{B}_n^m, \end{aligned} \tag{13}$$

and

$$\vec{B}(\vec{r}_{\mathrm{o}}, \omega_p) = \sum_{n,m \in L(p)} \varepsilon_n^m(\omega_p)\, \vec{B}_n^m(\vec{r}_{\mathrm{o}}, \omega_p). \tag{14}$$

For mantle induction studies, it is advantageous to work with the TFs which relate $\varepsilon_n^m(\omega_p)$ with a locally measured vertical component of the magnetic field, yielding

$$Z(\vec{r}_{\mathrm{o}}, \omega_p) = \sum_{n,m \in L(p)} \varepsilon_n^m(\omega_p)\, T_n^m(\vec{r}_{\mathrm{o}}, \omega_p). \tag{15}$$

Here, we follow Püthe & Kuvshinov (2014) and use $Z = -B_r$ and $T_n^m = -B_{n,r}^m$. We do not consider TFs that relate $\varepsilon_n^m(\omega_p)$ with the local tangential magnetic field components since they are less sensitive to the subsurface conductivity distribution (see Appendix C of this paper or Kuvshinov 2008). Instead, we used tangential magnetic field (and prescribed Earth's conductivity model) to estimate external source coefficients.

2.2 Estimation of the external coefficients

The $\varepsilon_{n,k}^m(\omega_p)$, $n, m \in L(p)$ coefficients at each frequency ω_p and for kth day are estimated by an iteratively reweighted least-squares (IRLS) regression with Huber weights using tangential magnetic field from $N(k)$ available observatories as

$$\min_{\widetilde{\boldsymbol{\varepsilon}}_k(\omega_p)} \left\| \mathbf{d}_{\tau,k}(\omega_p) - \mathrm{H}(\omega_p, \{\sigma\})\, \widetilde{\boldsymbol{\varepsilon}}_k(\omega_p) \right\|_{\text{Huber}},$$
$$k = 1, 2, ..., K, \quad p = 1, 2, ..., 6, \tag{16}$$

where, $\mathbf{d}_{\tau,k}$ is a data vector, $\widetilde{\boldsymbol{\varepsilon}}$ is a vector of the estimated external coefficients and H is a matrix of predicted tangential magnetic field. For example, for $p = 1$, they read

$$\mathbf{d}_{\tau,k}(\omega_1) = \begin{pmatrix} X_k^{\text{obs}}(\vec{r}_1, \omega_1) \\ X_k^{\text{obs}}(\vec{r}_2, \omega_1) \\ \vdots \\ X_k^{\text{obs}}(\vec{r}_N, \omega_1) \\ Y_k^{\text{obs}}(\vec{r}_1, \omega_1) \\ Y_k^{\text{obs}}(\vec{r}_2, \omega_1) \\ \vdots \\ Y_k^{\text{obs}}(\vec{r}_N, \omega_1) \end{pmatrix}, \qquad \widetilde{\boldsymbol{\varepsilon}}_k(\omega_1) = \begin{pmatrix} \widetilde{\varepsilon}_{1,k}^0(\omega_1) \\ \widetilde{\varepsilon}_{2,k}^0(\omega_1) \\ \vdots \\ \widetilde{\varepsilon}_{5,k}^2(\omega_1) \end{pmatrix},$$

$$\mathrm{H}(\omega_1, \{\sigma\}) = \begin{pmatrix} X_1^0(\vec{r}_1, \omega_1, \{\sigma\}) & X_2^0(\vec{r}_1, \omega_1, \{\sigma\}) & \dots & X_5^2(\vec{r}_1, \omega_1, \{\sigma\}) \\ X_1^0(\vec{r}_2, \omega_1, \{\sigma\}) & X_2^0(\vec{r}_2, \omega_1, \{\sigma\}) & \dots & X_5^2(\vec{r}_2, \omega_1, \{\sigma\}) \\ \vdots & & & \\ X_1^0(\vec{r}_N, \omega_1, \{\sigma\}) & X_2^0(\vec{r}_N, \omega_1, \{\sigma\}) & \dots & X_5^2(\vec{r}_N, \omega_1, \{\sigma\}) \\ Y_1^0(\vec{r}_1, \omega_1, \{\sigma\}) & Y_2^0(\vec{r}_1, \omega_1, \{\sigma\}) & \dots & Y_5^2(\vec{r}_1, \omega_1, \{\sigma\}) \\ Y_1^0(\vec{r}_2, \omega_1, \{\sigma\}) & Y_2^0(\vec{r}_2, \omega_1, \{\sigma\}) & \dots & Y_5^2(\vec{r}_2, \omega_1, \{\sigma\}) \\ \vdots & & & \\ Y_1^0(\vec{r}_N, \omega_1, \{\sigma\}) & Y_2^0(\vec{r}_N, \omega_1, \{\sigma\}) & \dots & Y_5^2(\vec{r}_N, \omega_1, \{\sigma\}) \end{pmatrix}.$$

Note that $X = -B_\vartheta$ and $Y = B_\varphi$ are north and east magnetic field components, respectively, $\vec{r}_j = (r_j, \vartheta_j, \varphi_j)$ position of jth observatory, X_n^m and Y_n^m tangential magnetic fields coming from numerical solutions of Maxwell's equations for a prior 3-D conductivity model $\{\sigma\}$ and for an excitation by a corresponding source (*cf.* eq. 13). These fields are calculated using volume integral equation solver *x3dg* (Kuvshinov 2008). The prior model comprises a 1-D conductivity model overlain by a thin shell of known laterally variable (2-D) conductance. We use the 1-D conductivity model by Grayver *et al.* (2017, Fig. 1a, black line) and 2-D conductance map (Fig. 1b) constructed according to TPXO8 bathymetry (Egbert & Erofeeva 2002) with laterally-varying sediment (Alekseev *et al.* 2015) and sea water (Grayver *et al.* 2016) conductivities. The heterogeneous shell allows us to account for the ocean effect. Note that N depends on k because N may vary from day to day due to the varying number and length of gaps at different observatories.

2.3 Estimation of TFs

With estimated $\widetilde{\varepsilon}_{n,k}^m(\omega_p)$, $n, m \in L(p)$, $k = 1, 2, ..., K$, TFs $T_n^m(\vec{r}_j, \omega_p)$ are estimated at each frequency ω_p and observatory j by a robust IRLS regression with Huber weights using vertical magnetic fields from $K(j)$ available days as

$$\min_{\widetilde{\mathrm{T}}_j(\omega_p)} \left\| \mathbf{d}_{\mathrm{Z},j}(\omega_p) - \mathcal{E}(\omega_p)\, \widetilde{\mathbf{T}}_j(\omega_p) \right\|_{\text{Huber}},$$
$$j = 1, 2, ..., N, \quad p = 1, 2, ..., 6, \tag{17}$$

where $\mathbf{d}_{\mathrm{Z},j}$ is a data vector, $\widetilde{\mathbf{T}}_j$ is a vector of the estimated TFs, and $\mathcal{E}$ is a matrix of external coefficients. For example, for $p = 1$, they read

$$\mathbf{d}_{\mathrm{Z},j}(\omega_1) = \begin{pmatrix} Z_1^{\text{obs}}(\vec{r}_j, \omega_1) \\ Z_2^{\text{obs}}(\vec{r}_j, \omega_1) \\ \vdots \\ Z_{\mathrm{K}}^{\text{obs}}(\vec{r}_j, \omega_1) \end{pmatrix}, \quad \widetilde{\mathrm{T}}_j(\omega_1) = \begin{pmatrix} \widetilde{T}_1^0(\vec{r}_j, \omega_1) \\ \widetilde{T}_2^0(\vec{r}_j, \omega_1) \\ \vdots \\ \widetilde{T}_5^2(\vec{r}_j, \omega_1) \end{pmatrix},$$

Table 1. Subsets of SH terms used to describe the external source at Sq periods $T_p = 24/p$ hr. Subscript and superscript of ε correspond to the degree n and order m, respectively. Bold values denote dominant terms.

T_1	–	ε_1^0	ε_2^0	ε_3^0	ε_1^1	$\boldsymbol{\varepsilon_2^1}$	ε_3^1	ε_4^1	ε_2^2	ε_3^2	ε_4^2	ε_5^2
T_2	ε_1^1	ε_2^1	ε_3^1	ε_4^1	ε_2^2	$\boldsymbol{\varepsilon_3^2}$	ε_4^2	ε_5^2	ε_3^3	ε_4^3	ε_5^3	ε_6^3
T_3	ε_2^2	ε_3^2	ε_4^2	ε_5^2	ε_3^3	$\boldsymbol{\varepsilon_4^3}$	ε_5^3	ε_6^3	ε_4^4	ε_5^4	ε_6^4	ε_7^4
T_4	ε_3^3	ε_4^3	ε_5^3	ε_6^3	ε_4^4	$\boldsymbol{\varepsilon_5^4}$	ε_6^4	ε_7^4	ε_5^5	ε_6^5	ε_7^5	ε_8^5
T_5	ε_4^4	ε_5^4	ε_6^4	ε_7^4	ε_5^5	$\boldsymbol{\varepsilon_6^5}$	ε_7^5	ε_8^5	ε_6^6	ε_7^6	ε_8^6	ε_9^6
T_6	ε_5^5	ε_6^5	ε_7^5	ε_8^5	ε_6^6	$\boldsymbol{\varepsilon_7^6}$	ε_8^6	ε_9^6	ε_7^7	ε_8^7	ε_9^7	ε_{10}^7

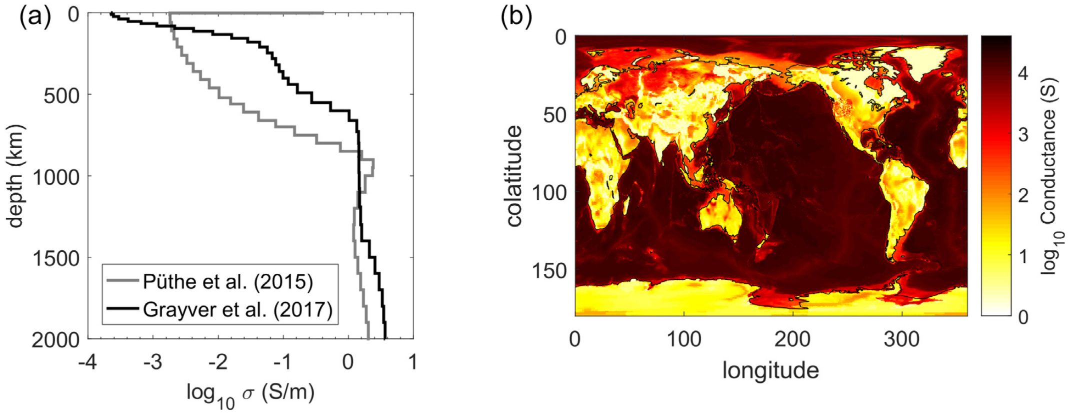

Figure 1. (a) Two independently acquired globally averaged 1-D conductivity models that were tested in the estimation of external coefficients. (b) Surface shell of laterally varying conductance in the upper part of the 1-D conductivity model.

$$\mathcal{E}(\omega_1) = \begin{pmatrix} \widetilde{\varepsilon}_{1,1}^0(\omega_1) & \widetilde{\varepsilon}_{2,1}^0(\omega_1) & \dots & \widetilde{\varepsilon}_{5,1}^2(\omega_1) \\ \widetilde{\varepsilon}_{1,2}^0(\omega_1) & \widetilde{\varepsilon}_{2,2}^0(\omega_1) & \dots & \widetilde{\varepsilon}_{5,2}^2(\omega_1) \\ \vdots & & & \\ \widetilde{\varepsilon}_{1,K}^0(\omega_1) & \widetilde{\varepsilon}_{2,K}^0(\omega_1) & \dots & \widetilde{\varepsilon}_{5,K}^2(\omega_1) \end{pmatrix}.$$

The selection of appropriate days for TFs determination will be discussed in the next section. Note that the dependence of K on j means that the total number of the selected days, K, depends on the number and length of gaps at observatory j.

3 DATA SELECTION

We use hourly means of magnetic field recordings from a global network of permanent geomagnetic observatories. The recordings come from a quality-controlled data set provided by the British Geological Survey (BGS) (Macmillan & Olsen 2013) and cover a period from 1997 to 2016. In order to avoid disturbances from equatorial and auroral electrojets, we exclude data from observatories $\pm 5^\circ$ equatorward of the dip equator and poleward of $\pm 55^\circ$ quasi dipole latitude. Positions of the remaining 136 mid-latitude observatories are shown in Fig. 2(a). Codes, names and coordinates of these observatories are summarized in Appendix D.

Morphology of diurnal magnetic variations varies daily, seasonally, and annually depending on solar magnetic activity and the orbital position of Earth. In order to mitigate these effects, we work with single day magnetic field recordings when estimating source coefficients.

Furthermore, we choose magnetically quiet days during or close around equinoxes (March–April, September–October) when the source current has a symmetric double vortex structure (compare Fig. 3), thus allowing us to parametrize it by a relatively small number of SH terms as specified in eq. (12). In contrast, the shape of the current function during solstice months (compare Fig. 4) looses the symmetry and requires more spatial modes to fully accommodate the increased complexity.

In order to support the idea to use data on magnetically quiet, equinoctial days, we perform the following model study. We determine daily source coefficients $\widetilde{\varepsilon}_{n,k}^m$—using an approach described in Section 2.—for an entire span of 20 yr, that is for disturbed and quiet days from all seasons. Note that in order to isolate Sq signal in the data, we implement the procedure described in Yamazaki & Maute (2017). We start by determining a local level of no variations, called the true zero baseline. We define the level of no variations as a 3-hr average of night-time data (0:30–2:30 local time). This is done for each day, station and magnetic field component. Due to the slowly varying magnetospheric currents, the true zero baselines of consecutive days may differ and the samples of successive days may experience jumps. To correct for this, we determine and remove the non-cyclic variation, which is defined as a linear trend between the first and last sample of a day in local time. Additionally, we correct X magnetic field component for the disturbed storm time (Dst) field.

Afterwards, we evaluate the coefficient of determination R^2 between observed and predicted fields for kth day as

$$R_k^2(M, \omega_p) = 1 - \frac{\sum_{j=1}^{N} |M_k^{\mathrm{obs}}(\vec{r}_j, \omega_p) - M_k(\vec{r}_j, \omega_p, \{\sigma\})|^2}{\sum_{j=1}^{N} |M_k^{\mathrm{obs}}(\vec{r}_j, \omega_p) - \overline{M}_k^{\mathrm{obs}}(\omega_p)|^2}, \tag{18}$$

where M stands for either X, Y or Z magnetic field component, $\overline{M}$ denotes the mean of observed fields over N stations

$$\overline{M}_k^{\mathrm{obs}}(\omega_p) = \frac{1}{N} \sum_{j=1}^{N} M_k^{\mathrm{obs}}(\vec{r}_j, \omega_p), \tag{19}$$

and predicted fields are calculated as

$$M_k(\vec{r}_j, \omega_p, \{\sigma\}) = \sum_{n,m \in L(p)} \widetilde{\varepsilon}_{n,k}^m(\omega_p) M_n^m(\vec{r}_j, \omega_p, \{\sigma\}). \tag{20}$$

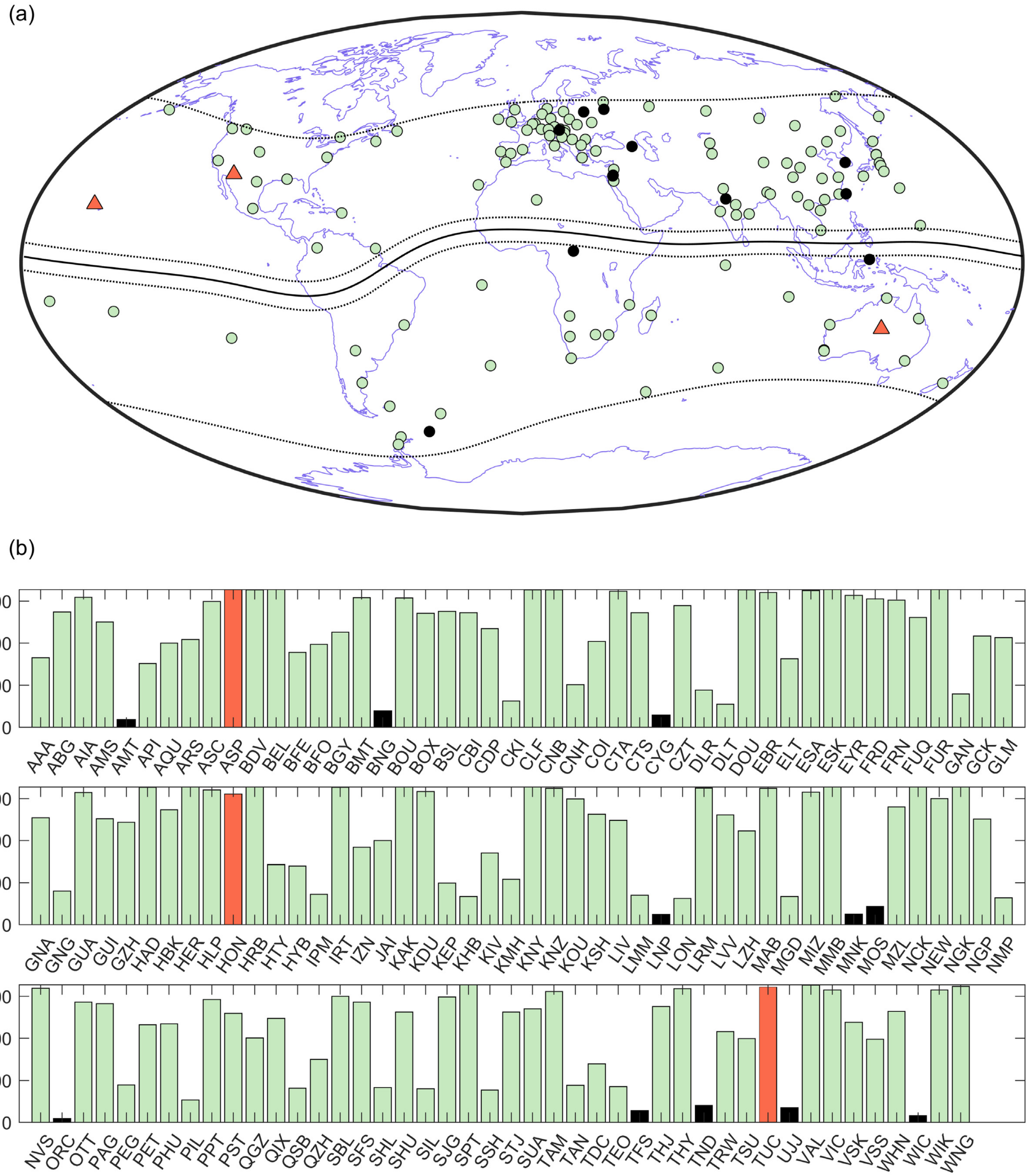

Figure 2. (a) Geomagnetic observatories $\pm 5^{\circ}$ poleward of the dip equator and equatorward of $\pm 55^{\circ}$ quasi dipole latitude that are available from the BGS data set (more details are provided in Appendix D). Black circles indicate observatories with less than 50 magnetically quiet, equinoctial days. Data from the observatories denoted by the orange triangles were inverted in this study for the mantle conductivity. (b) Number of available days, K, per observatory. Black and orange bars correspond to observatories from (a).

Here, similarly to Section 2.2, M_n^m are numerical solutions of Maxwell's equations for a prior 3-D conductivity model $\{\sigma\}$ and a corresponding source. R^2 quantifies goodness of fit over all observatories and has values between zero (no fit) and one (perfect fit).

In Fig. 5, we present R^2 values for X, Y and Z components for all days (in grey circles) versus for equinoctial days (in red pluses) in a 20-yr time span with respect to a 48-hr average (including 12 hr before and after the day) of magnetic activity given by the *aa* index (Mayaud 1980). In what follows, we denote the 48-hr average

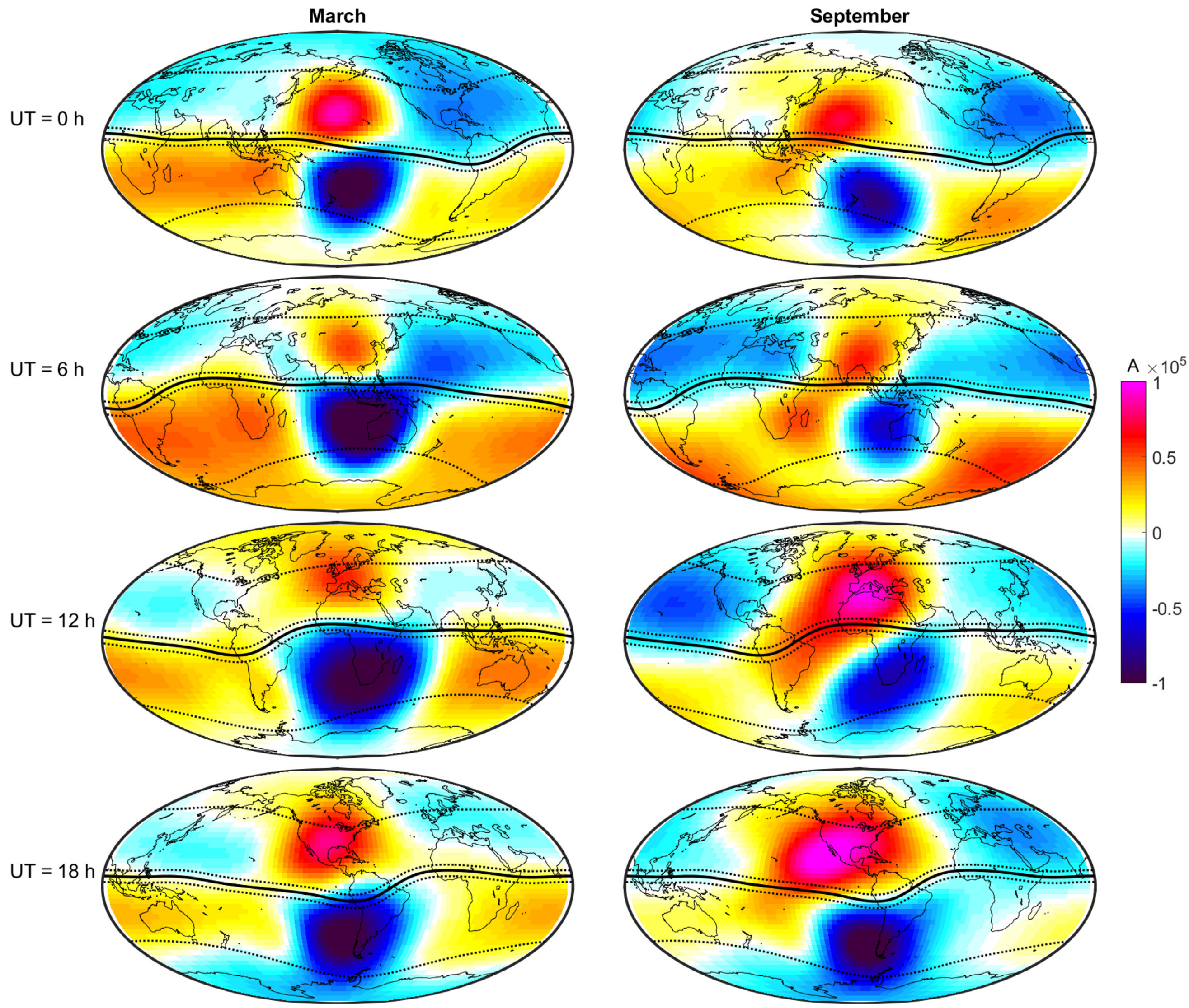

Figure 3. Snapshots of the Sq current function on equinoctial (and magnetically quiet) days in year 2009: March 17th and September 26th. Bold solid black line depicts the dip equator and light black dashed lines show ±5° poleward of the dip equator and equatorward ±55° quasi dipole latitude. The current function in time domain was estimated using eq. (9) as $\Psi(\vec{r}, t) = \mathrm{Re}\left[\sum_{p=1}^{6} \Psi(\vec{r}, \omega_p) \exp(\mathrm{i}\omega_p t)\right]$.

of the *aa* index by $\widehat{aa}$. Black and red lines in the figure represent the mean of R^2 values on all and equinoctial days, respectively. As expected, the goodness of fit decreases with increasing p and increasing magnetic activity. Additionally, the fit on equinoctial days is better than on other days for $p = 2, 3, 4$, whereas for $p = 1, 5, 6$ the average fit is nearly identical for all seasons. Finally, the fit is systematically better for Y component compared to X and Z components for all p.

The decreased fit at shorter periods is expected because of lower signal amplitudes and, consequently, smaller signal-to-noise ratio. In addition, shorter periods require higher degree/order SH to describe the source (*cf*. Table 1). However, sparse distribution of the observatories (*cf*. Fig. 2a) hinders reliable estimation of external coefficients corresponding to higher degree/order SH terms.

Similarly, the decrease of fit with increasing magnetic activity can be attributed to the inability of the chosen parametrization to describe a more complex source geometry during the disturbed days. Lower fit during other months than equinoctial is also expected, since the orbital position of the Earth affects the shape and magnitude of the Sq source (*cf*. Figs 3 and 4) and makes the chosen source parametrization during non-equinoctial months less suitable.

Furthermore, X component is known to be the most susceptible to the magnetospheric disturbances compared to Y and Z components (Yamazaki & Maute 2017), which might be the cause for the lower fit in X component. Lower (compared with Y) fit in Z probably shows that Z is sensitive to locally heterogeneous mantle, whereas a global 1-D conductivity distribution in the mantle was assumed for the source determination. The latter observation supports our

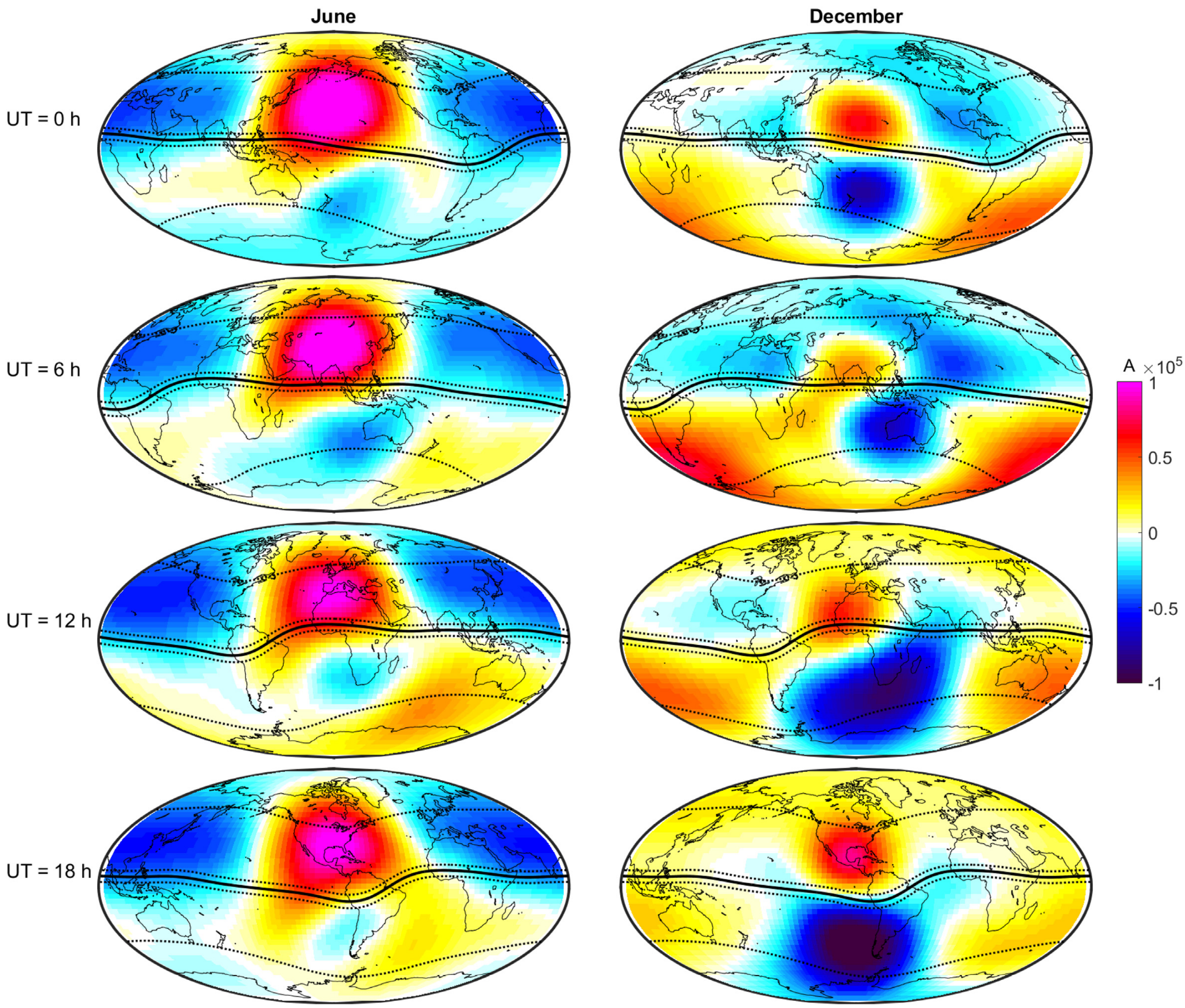

Figure 4. Same as in Fig. 3 but for solstice days in year 2009: June 10th and December 22nd.

efforts to estimate and invert global-to-local TFs, $T_n^m(\vec{r}_j, \omega_p)$, in order to detect local deviations of conductivity from the global 1-D distribution.

In summary, working with magnetically quiet days during equinoctial months is preferable. The last question we have to address before proceeding with the estimation of TFs is how to formally define magnetically quiet and disturbed days. According to the definition by ISGI (2018), the day is considered quiet if $\widehat{aa} < 13$ nT. In this study, we can decrease this value as long as we still have enough data to estimate TFs reliably. The adopted source parametrization consists of 12 spatial modes per period, establishing a lower bound on a number of days that are necessary to reliably determine TFs at a given observatory. Fig. 6 displays number of equinoctial days between 1997 and 2016 sorted by the $\widehat{aa}$ index up to the threshold of 13 nT. We see a pronounced peak at $\widehat{aa}$ between 5 and 6 nT with a gradual decay towards smaller and larger values of $\widehat{aa}$. The total number of equinoctial days below 7 nT is 327, which should suffice for reliable estimation of TFs. Therefore, we will use equinoctial days with $\widehat{aa} < 7$ nT. Note that the actual number of quiet, equinoctial days included in the analysis varies with an observatory. Fig. 2(b) illustrates this by showing the number of available quiet equinoctial days per observatory. To facilitate statistical stability of the TFs, we excluded observatories with less than 50 quiet, equinoctial days (depicted in black in Fig. 2).

4 RESULTS

4.1 External coefficients

Following previous section, we estimated external source coefficients $\varepsilon_n^m(\omega_p)$ for 327 quiet, equinoctial days. Fig. 7 shows the number of observatories, N, used at each selected day; it is seen that N indeed varies from day to day, but more than 75 observatories are always present in the analysis. Fig. 8 depicts F10.7 index which specifies solar activity in the selected years. This plot illustrates the fact that the number of suitable days increases during periods of low solar activity. Fig. 9 demonstrates the magnitudes of corresponding external coefficients obtained using 1-D model by Grayver *et al.* (2017). Coefficients of degree $n = p + 1$ and order $m = p$, that are expected to be dominant (*cf.* Table 1), are depicted in dark grey. For the periods of 24, 12, 8 and 6 hr these coefficients indeed have the largest magnitudes, but for the periods of 4.8 and 4 hr the largest

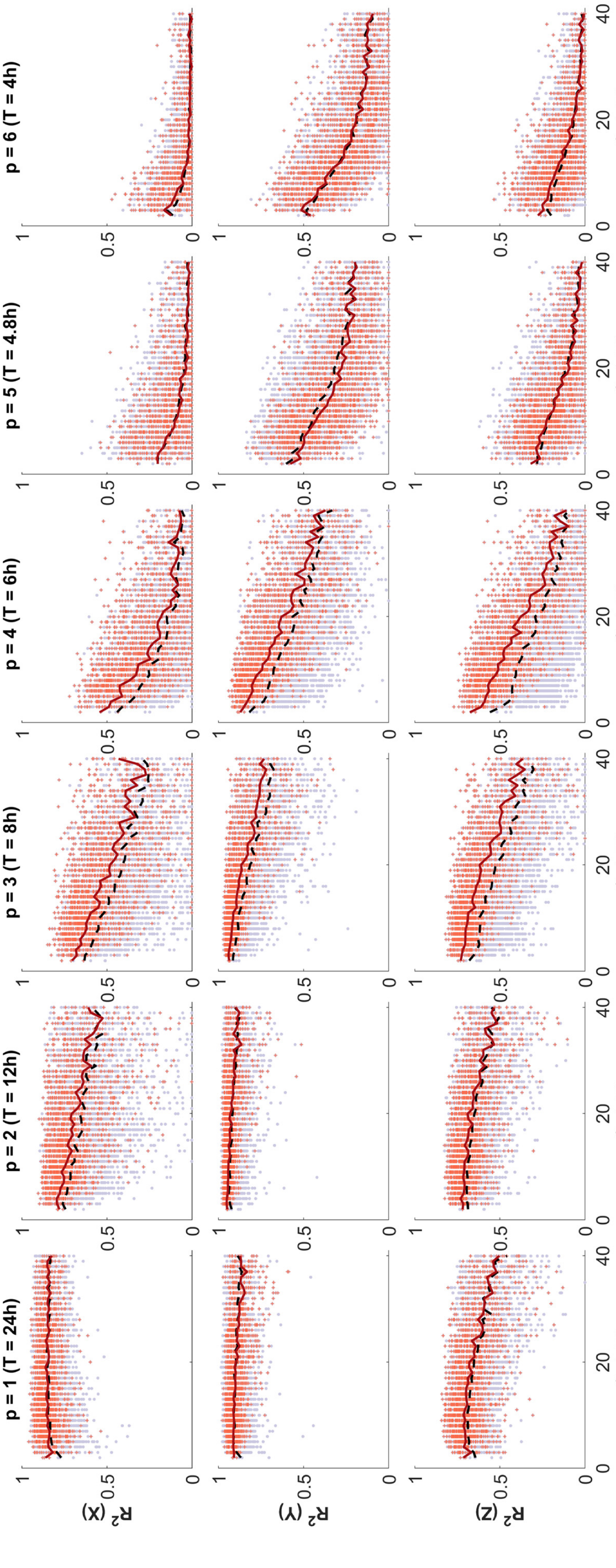

Figure 5. Coefficient of determination, R^2 (eq. 18), for six time harmonics of X, Y and Z components for all days (grey circles) and equinoctial days (red pluses) in a 20-yr time span. The results are shown with respect to a 48-hr average (including 12 hr before and after the chosen day) of magnetic aa index. Black dashed and red solid lines are mean values of all and equinoctial values, respectively.

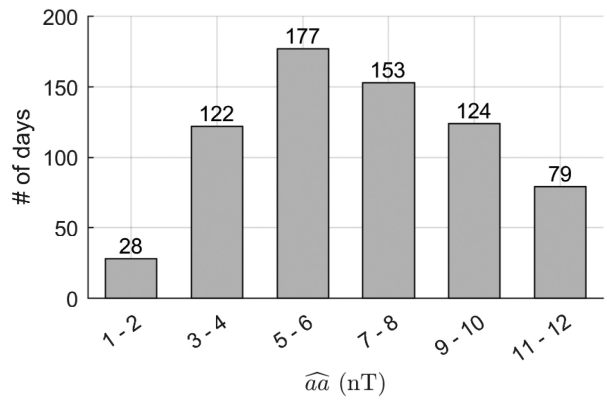

Figure 6. Number of quiet, equinoctial days between 1997 and 2016 sorted by a 48-hr average *aa* index.

coefficients are of degree and order p. Shorter periods require higher degree/order SH to describe the source, but with the given spatial distribution of the observatories it becomes difficult to estimate the external coefficients reliably. This is likely the reason that there is no apparent dominant coefficient at the shortest periods.

The external source coefficients, $\varepsilon_n^m(\omega_p)$, are sensitive to the prior conductivity model used for their estimation. We evaluate relative differences in the estimated coefficients for each day k as

$$\mathrm{diff}(\omega_p, k) = \frac{|\widetilde{\varepsilon}^{p,(1)}_{p+1,k}(\omega_p) - \widetilde{\varepsilon}^{p,(2)}_{p+1,k}(\omega_p)|}{|\widetilde{\varepsilon}^{p,(1)}_{p+1,k}(\omega_p)|} \cdot 100\%, \tag{21}$$

where superscripts (1) and (2) correspond to different conductivity models. Fig. 1(a) shows two global 1-D models we tested. One is the model by Grayver *et al.* (2017) obtained by joint inversion of tidal magnetic signals and magnetospheric C-responses, and another—the model by Püthe *et al.* (2015a) obtained by inversion of magnetospheric C-responses only. Note that different data sets and different algorithms were used to obtain the corresponding C-responses. Fig. 10 shows the acquired relative differences on the selected days, which increase with increasing p, i.e., with decreasing period. Averaged over 327 d, the differences are 6.5 per cent for $p = 1$, 8.0 per cent for $p = 2$, 8.7 per cent for $p = 3$, 9.1 per cent for $p = 4$, 11.6 per cent for $p = 5$, and 9.8 per cent for $p = 6$.

4.2 Estimated TFs

We estimated TFs and their uncertainties at 125 locations (green circles in Fig. 2a). For 24 hr and subsequent harmonics, 11 and 12 T_n^m were estimated, respectively (see Table 1). For brevity, we will only analyse the terms T_n^m with $n = p + 1$ and $m = p$ which are expected to be dominant.

Before presenting the results, it is important to note that

(i) In contrast to Q-responses (Appendix E), T_n^m (of any n and m) depend on r, ϑ and φ;

(ii) Dependence of T_n^m on ϑ and φ is mostly governed by degree n and order m of the corresponding SH. It becomes clear if one considers T_n^m at the surface of 1-D Earth's conductivity model. In this case – in accordance with eqs (15) and (E3) – T_n^m are written as

$$T^m_{n,1D}(r = a, \vartheta, \varphi, \omega) = [n - (n+1)Q_n(\omega)]S_n^m(\vartheta, \varphi). \tag{22}$$

(iii) Since Q_n varies insignificantly in the considered period range (see Table E1), eq. (22) suggests that T_{p+1}^p increase in magnitude for decreasing periods.

Fig. 11 shows real and imaginary parts of the T_{p+1}^p TFs. Circles show estimated TFs, and maps – TFs that are modelled using a prior 3-D conductivity model (described in Section 2.2). Note that the modelling was performed on a 1° × 1° grid. It follows from the figures that the spatial patterns and the amplitudes of the estimated and modelled TFs are in concert with eq. (22), however, the presence of non-uniform oceans and continents of laterally variable conductance evidently makes a picture more complicated.

4.3 Ocean effect in the TFs

Fig. 12 quantifies the ocean effect in TFs by presenting differences between the TFs calculated for a prior 3-D model (with non-uniform oceans and continents) and 'local normal' TFs. The local normal TFs were calculated using a global 1-D model overlain by a uniform thin shell with a value of conductance at a given point. As expected, the difference is the largest in coastal regions where significant contrasts in surface shell conductance exist (*cf.* Fig. 1b). The effect increases in strength at shorter periods and is comparable in magnitude with the TFs themselves (*cf.* Fig. 11). Therefore, at least at coastal and island observatories, non-uniform oceans and continents should be accounted for during modelling and inversion of TFs.

4.4 Influence of a prior conductivity model on TFs estimation

In this section, we assess the sensitivity of the estimated TFs to the conductivity model used to determine the external source coefficients. The results are shown in a form of relative differences in the estimated TFs

$$\mathrm{diff}(\vec{r}_j, \omega_p) = \frac{|\widetilde{T}^{p,(1)}_{p+1}(\vec{r}_j, \omega_p) - \widetilde{T}^{p,(2)}_{p+1}(\vec{r}_j, \omega_p)|}{|\widetilde{T}^{p,(1)}_{p+1}(\vec{r}_j, \omega_p)|} \times 100\,\text{per cent}. \tag{23}$$

As in eq. (21), superscripts (1) and (2) correspond to the models by Grayver *et al.* (2017) and Püthe *et al.* (2015a), respectively.

A comparison between TFs estimated from the two different sets of source coefficients is shown in Fig. 13. One can see that the relative differences increase with the decreasing period, and at some locations the differences are as high as 30 per cent. Averaged over the entire globe, the differences are 7.1 per cent at 24 r, 9.7 per cent at 12 hr, 10.3 per cent at 8 hr, 11.0 per cent at 6 hr, and 11.8 per cent at both 4.8 and 4 hr. This result suggests that the mantle model used to estimate the source coefficients should be iteratively updated with a model obtained from inversion of the estimated TFs.

4.5 Effect of ocean tidal magnetic signals on TFs and its correction

Since our concept assumes that the source currents are of external origin, magnetic fields generated in the oceans can contaminate TFs at diurnal and semi-diurnal periods. Although most tidal constituents have slightly different periodicity than the daily variations (see Table F1), semi-diurnal and diurnal tidal magnetic signals overlap with daily variations in single day recordings. Therefore, we correct for ocean tidal magnetic signals in the data as described in Guzavina *et al.* (2018). Short summary on how tidal signals are calculated can be found in Appendix F.

Fig. 14 demonstrates the relative differences (see eq. 23) in TFs estimated from original data and data corrected for the ocean tidal magnetic signals. The tidal correction mostly influences TFs at

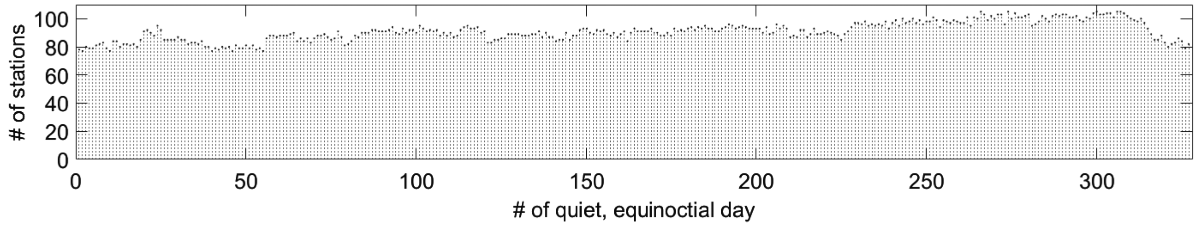

Figure 7. Number of available mid-latitude observatories, *N*, on 327 quiet, equinoctial days used to estimate external coefficients. Note that the number of stations varies daily due to gaps in data.

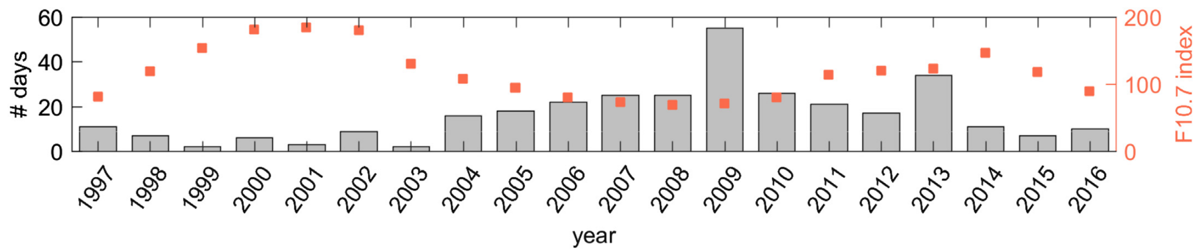

Figure 8. Number of quiet, equinoctial days (bars) against yearly averaged F10.7 index (squares, Space Weather Canada 2019) in a 20 yr time span.

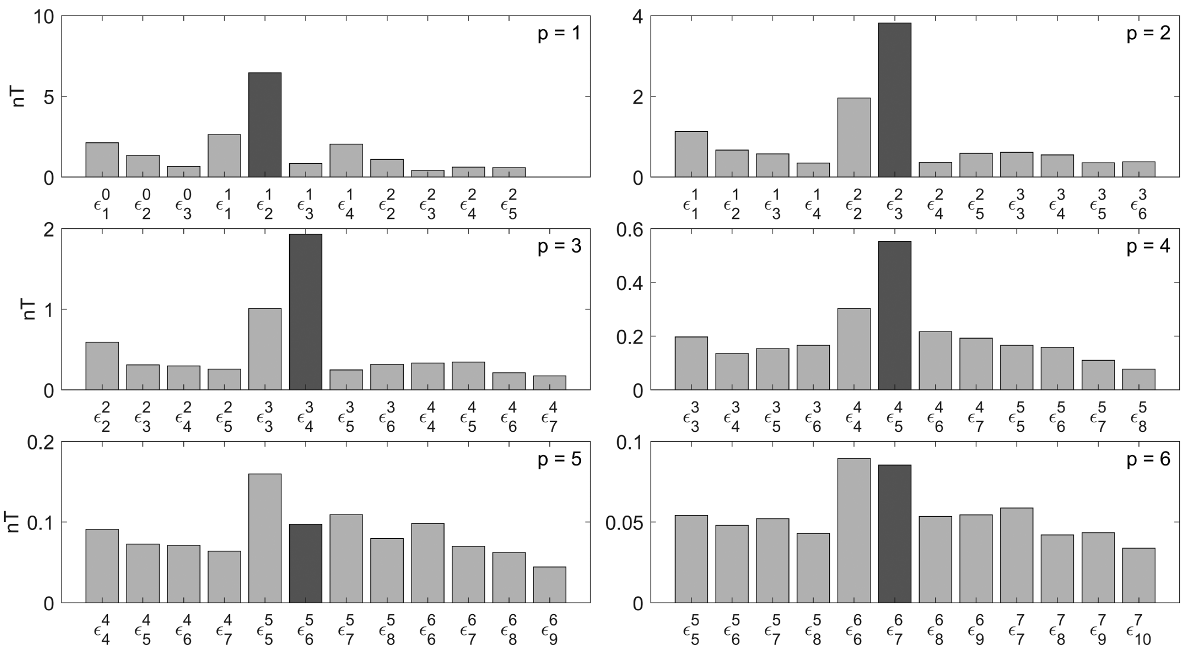

Figure 9. Magnitudes of external source coefficients averaged over 327 quiet, equinoctial days. Dark grey bars indicate coefficients of degree $n = p + 1$ and order $m = p$, that are expected to be dominant (*cf.* Table 1).

coastal and island observatories. This influence is visible at both periods but is the most prominent at 12 hr, where TFs at certain observatories can change up to 50 per cent. This behaviour is expected, since the semi-diurnal M_2 tide has the largest magnitude among the considered tidal constituents listed in Table F1. The average differences are 2.6 per cent at 24 hr and 13.1 per cent at 12 hr. Assuming that the tidal predictions are trustworthy, this result suggests that correcting the data for ocean tidal signals prior to estimation of TFs is justified.

5 INVERSION

In this section, we aim to show that the TFs carry local information about conductivity structure in different geological settings. For this purpose, we select a deep inland (Alice Springs, ASP), a close to the coast (Tucson, TUC) and an island (Honolulu, HON) observatories and invert for 1-D conductivity profiles at these locations. Note that we still use a 3-D forward operator based on the *x3dg* code to account for the ocean effect.

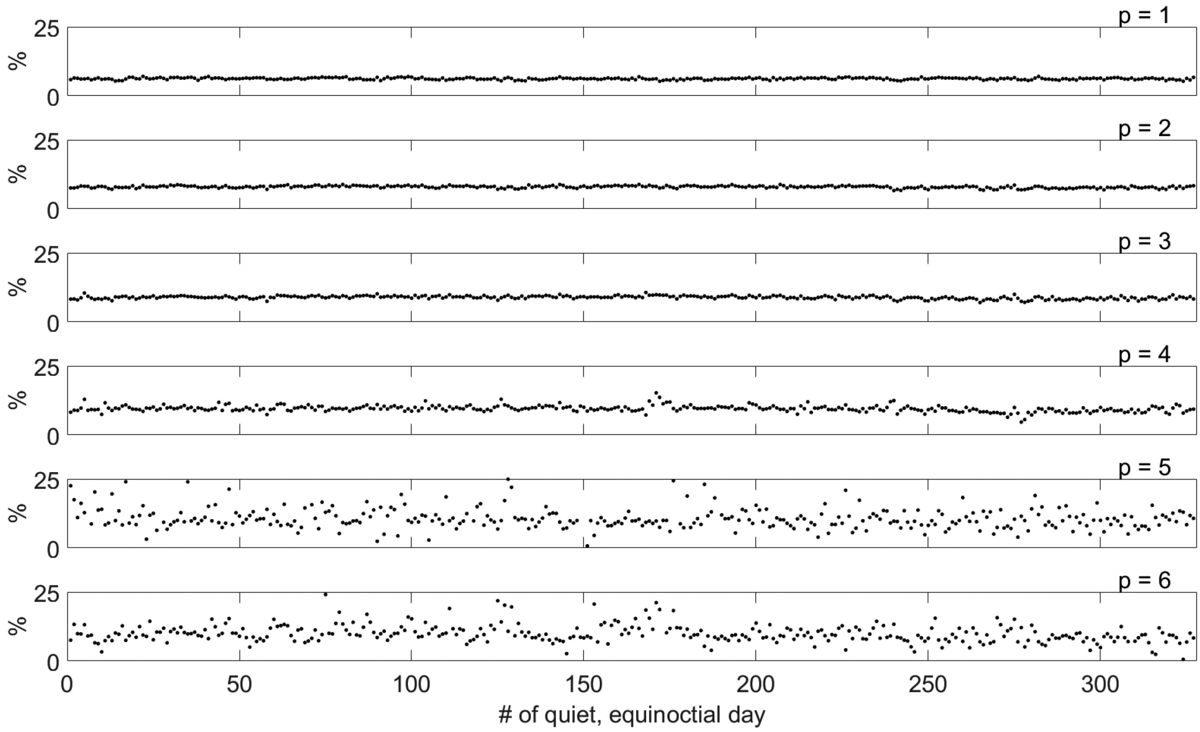

Figure 10. Relative differences (eq. 21) between dominant external source coefficients obtained using model by Püthe *et al.* (2015a) and model by Grayver *et al.* (2017). Models are depicted in Fig. 1(a).

5.1 Inversion procedure

The 1-D profile at each location is subdivided from the surface down to the core–mantle boundary (CMB) at 2900 km into 26 layers. We fix the core conductivity to $\sigma = 10^5$ S m^{-1} and use a homogeneous mantle of 0.2 S m^{-1} as a starting model.

We use a stochastic optimization technique Covariance Matrix Adaption Evolution Strategy (CMAES, Hansen & Ostermeier 2001) that is capable of escaping local minima and only weakly depends on the starting model (e.g. Grayver & Kuvshinov 2016). Additionally, it allows us to use arbitrary norms for data misfit and model regularization terms.

In short, CMAES draws $\lambda = 4 + 3\ln M$ models at each iteration using the current multivariate normal distribution, where M defines the number of unknown model parameters $\mathbf{m} = (\mathrm{m}_1, \mathrm{m}_2, ..., \mathrm{m}_M)$. Here, $\mathbf{m} = \left(\log(\sigma_1), \log(\sigma_2), ..., \log(\sigma_M)\right)$ describes conductivity of the corresponding layer (in our case, $M = 26$). Next, the cost function, $\phi(\mathbf{m}) = \phi_d(\mathbf{m}) + \beta\phi_m(\mathbf{m})$, is evaluated. Then, the distribution mean and covariance matrix are updated until one of the termination criteria is satisfied.

The maximum posterior probability model, $\mathbf{m}_{\mathrm{MAP}}$, is determined by solving the optimization problem

$$\mathbf{m}_{\mathrm{MAP}} = \underset{m}{\operatorname{argmin}} \, [\phi_d(\mathbf{m}) + \beta\phi_m(\mathbf{m})] \,, \tag{24}$$

where data term, ϕ_d, is given by

$$\phi_d(\mathbf{m}) = \frac{1}{2}\sum_{p=1}^{6}\left|\frac{T^{\mathrm{obs}}(\omega_p) - T^{\mathrm{mod}}(\mathbf{m}, \omega_p)}{\delta T^{\mathrm{obs}}(\omega_p)}\right|^2 \tag{25}$$

and model term, ϕ_m, is given by

$$\phi_m(\mathbf{m}) = \frac{1}{w}\sum_{i=1}^{M}\left|\nabla m_i\right|^w. \tag{26}$$

Here, β is regularization parameter, w model regularization norm, T^{obs} estimated dominant TFs with corresponding errors δT^{obs} and T^{mod} modelled dominant TFs. In this study, the model regularization norm value $w = 1.5$ was used. For further details on the method, the reader is referred to Grayver & Kuvshinov (2016) and Hansen & Ostermeier (2001).

5.2 Results

Fig. 15 shows the best-fitting conductivity models obtained at ASP, HON and TUC along with the Grayver *et al.* (2017) model and conductivities of dry and wet Olivine assuming $T \approx 1380$ °C at the 80 km deep lithosphere–asthenosphere boundary (Katsura & Yoshino 2015). The corresponding fit between observed and modelled responses is depicted in Fig. 16. The trade-off between data fit and regularization was determined by performing an L-curve analysis.

Fig. 15 shows lack of resolution in the top 100 km that is evident from generally quite high conductivity values at all observatories. The poor sensitivity at these depths is likely due to both purely inductive nature of the TFs as well as absence of periods shorter than 4 hr.

Despite their simplistic nature, the retrieved conductivity profiles provide good data fit (Fig. 16) and reveal a few interesting aspects. For HON, we observe good agreement between our and Grayver *et al.* (2017) model in the depth range of 150–300 km. This is noteworthy, since Grayver *et al.* (2017) model was obtained from a different source and independent data sets. The obtained profile at HON gets more conductive below 300 km than the global average profile, which could potentially be caused by a combination of increased temperatures, water, and melt associated with the Hawaiian mantle plume (Lizarralde *et al.* 1995; Simpson *et al.* 2000; Constable & Heinson 2004). Potentially, the model and data fit at this

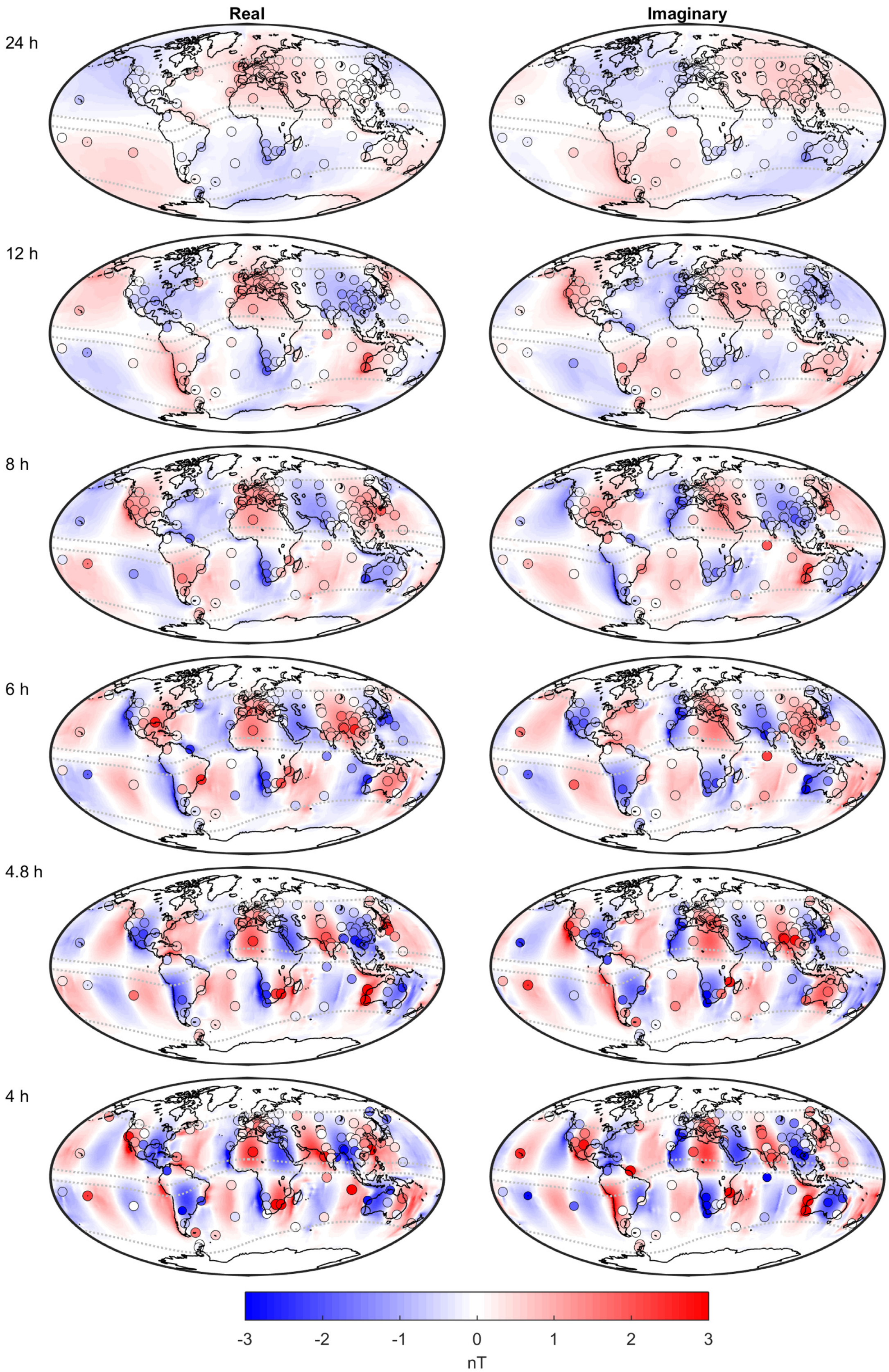

Figure 11. Estimated dominant TFs (circles, eq. 17) depicted on top of the dominant TFs calculated for a prior 3-D conductivity model (maps).

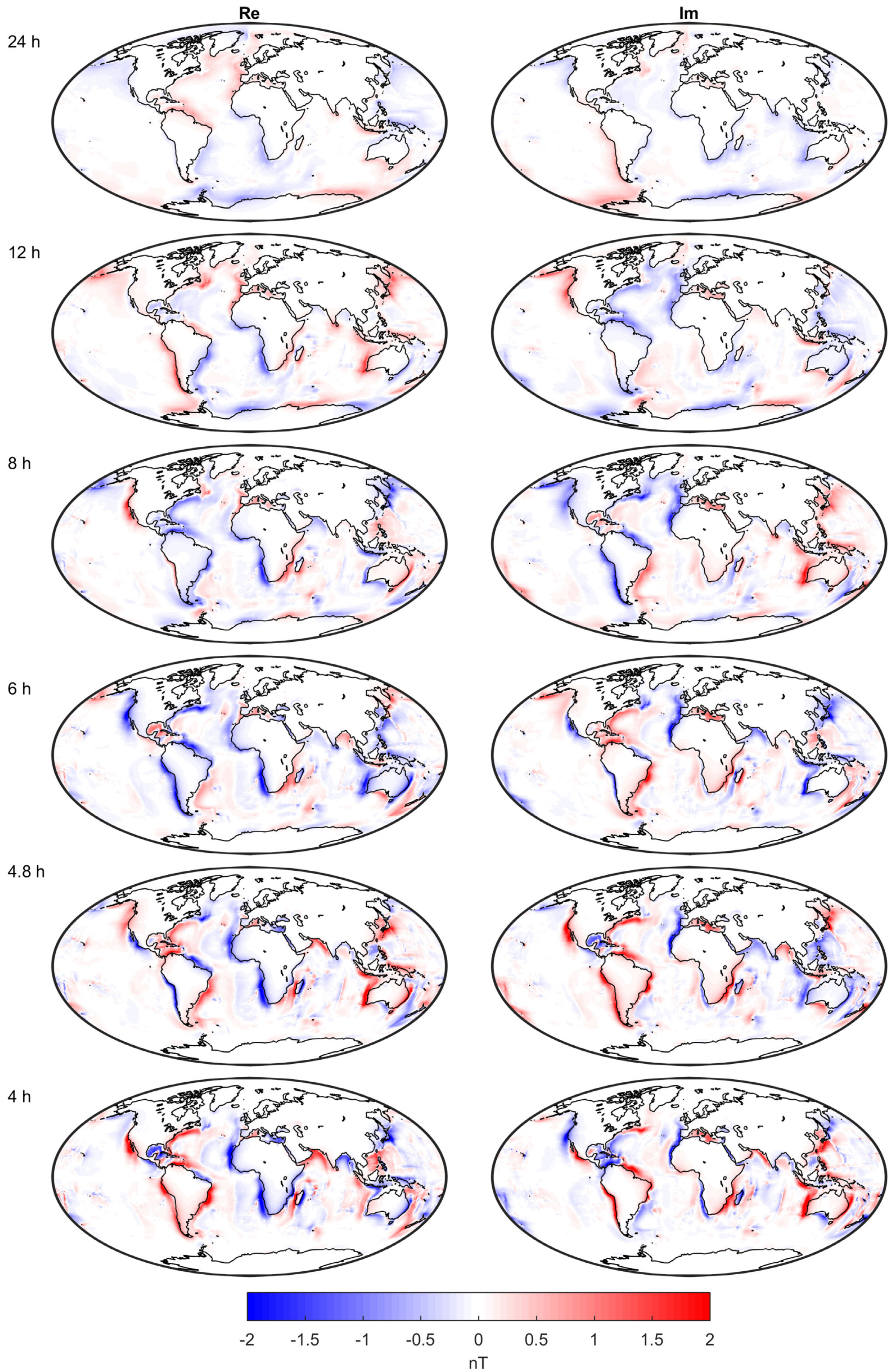

Figure 12. Ocean effect in the dominant TFs. Shown is a difference between the TFs calculated for a prior 3-D model (with non-uniform oceans and continents) and 'local normal' TFs (see Section 4.3 for more details). Left- and right-hand columns correspond to real and imaginary parts, respectively.

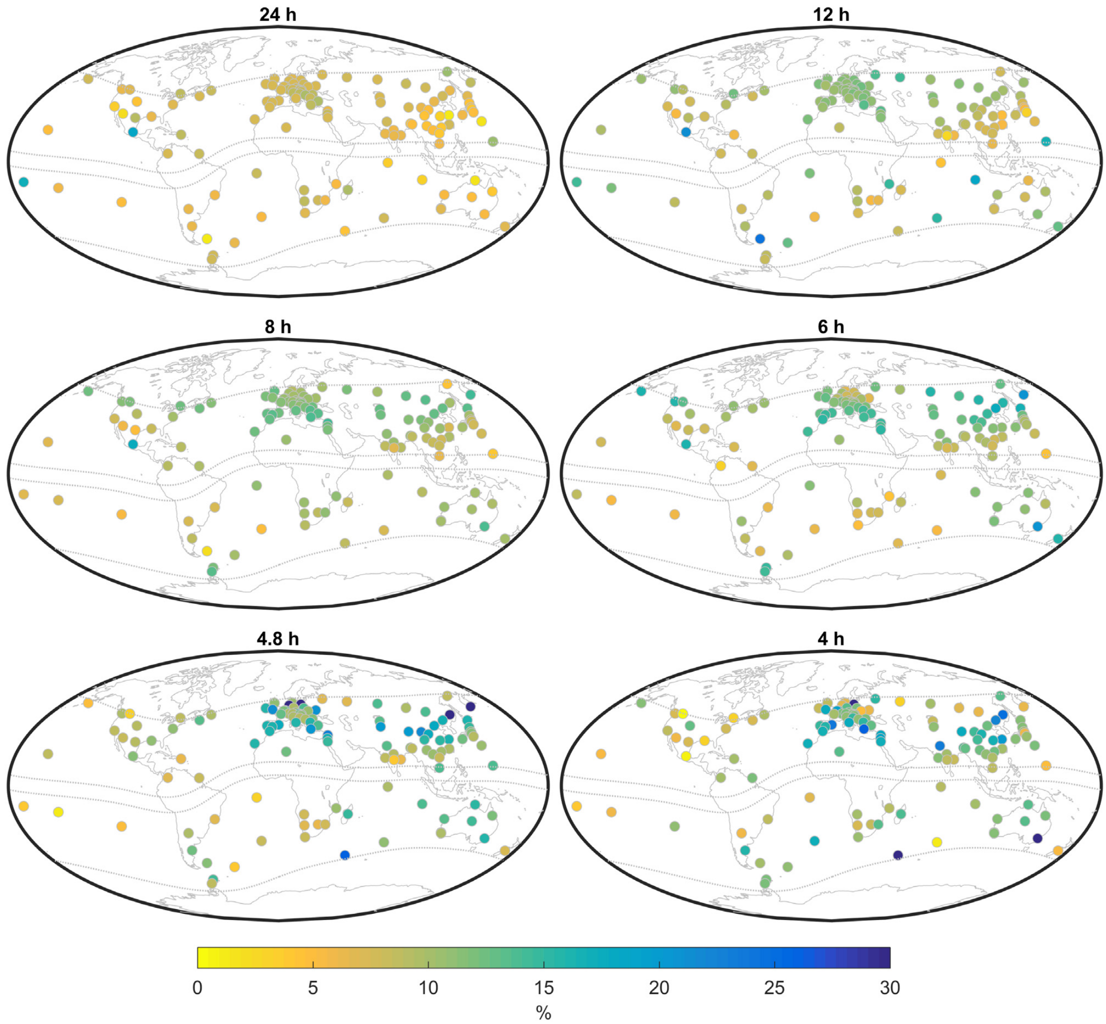

Figure 13. Relative differences (eq. 23) between TFs obtained using model by Püthe *et al.* (2015a) and model by Grayver *et al.* (2017). Models are depicted in Fig. 1(a).

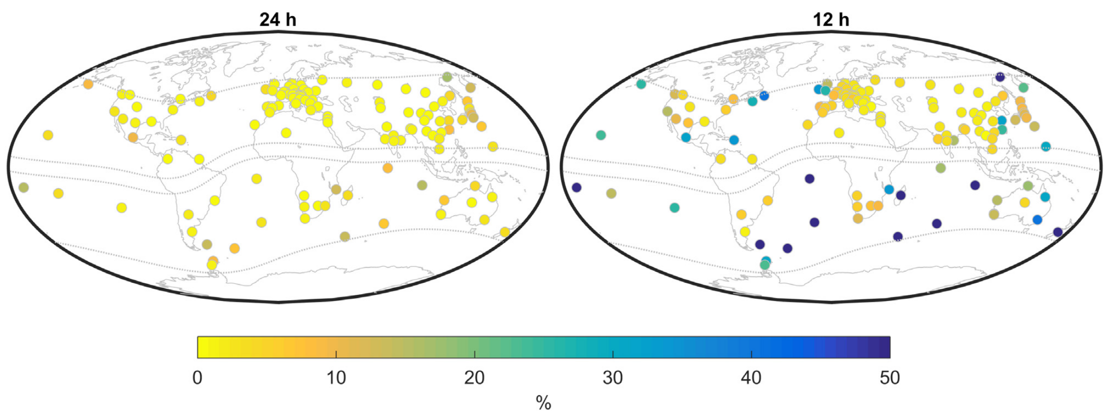

Figure 14. Relative differences (eq. 23) between TFs estimated from original data and data corrected for the ocean tidal magnetic signals.

location could be improved through using higher resolution grid (we used $0.25^\circ \times 0.25^\circ$) to incorporate the complex bathymetry and coastline more accurately.

Next, TUC is located on a younger continental lithosphere in the region of active crust extension (Neal *et al.* 2000). The conductivity values retrieved for the upper mantle below TUC (10^{-2}–10^{-1} S m^{-1} at 200–400 km) match previous model by Egbert & Booker (1992) and were explained by the presence of partial melt from the subduction, upwelling and melting of the Farallon plate (Hirth *et al.* 2000).

As for ASP, it is located in the orogen zone created during a major intraplate mountain building episode that dates back to Palaeozoic era (245–570 Ma, Haines *et al.* 2001). Our model is in good agreement with the Australian hemisphere model by Campbell *et al.*

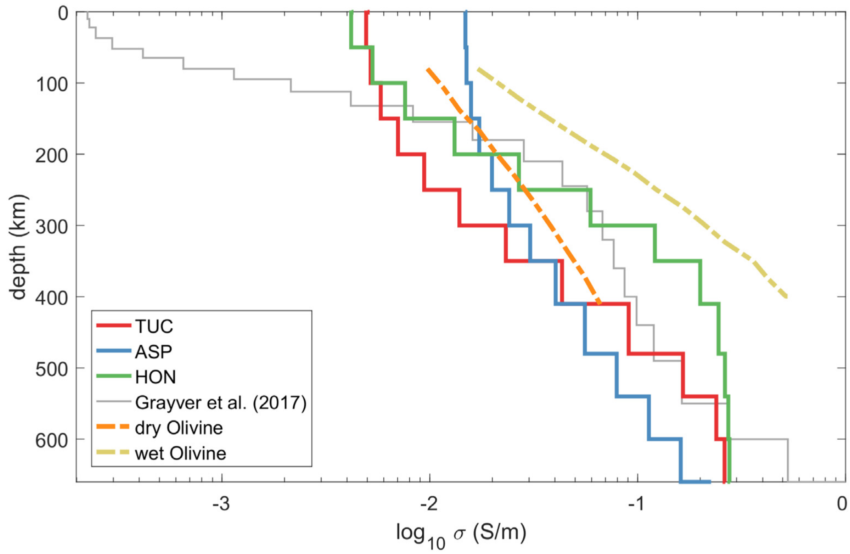

Figure 15. Best-fitting conductivity models obtained in this study compared to the global model of Grayver *et al.* (2017) and conductivity profiles of dry and wet olivine (max. saturation) derived from the laboratory measurements (Yoshino *et al.* 2006; Katsura & Yoshino 2015).

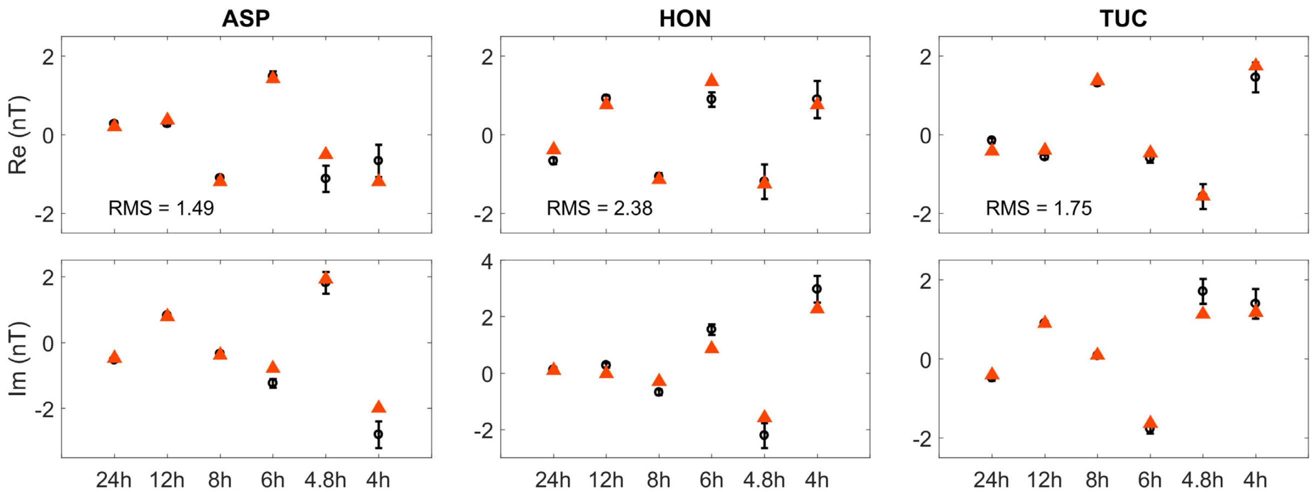

Figure 16. Observed (circles with errorbars) and best-fitting model TFs (red triangles) for ASP, HON and TUC observatories. The observed TFs were determined using eq. (17).

(1998). Campbell *et al.* (1998) worked with Sq variations on quiet days, and his model also has a rather smooth appearance with no indication of 410 and 520 km discontinuities. Furthermore, our model fits well within the range of acceptable models for Central Australia established by Lilley *et al.* (1981) that assumed a continental upper mantle composition and geotherm.

There are pronounced differences between 1-D profiles obtained for the selected locations. These variations most likely reflect large-scale conductivity variations in the upper mantle. However, since we neglected lateral variations of the conductivity at depths in our 1-D inversions, one may argue that some of the variability in the 1-D profiles are due to unaccounted 3-D effects. While this possibility cannot be ruled out completely, we believe that the 1-D approach is a reasonable first order approximation. First of all, obtained conductivity profiles match previous studies we refer to, some of them based on alternative and independent data. Second, sensitivity kernels for a point vertical magnetic field measurement due to the Sq source are local in nature (Pankratov & Kuvshinov 2010), decaying exponentially as we move away from the observation site. Therefore, the TFs we used are, to first order, sensitive to the radial conductivity underneath the observatory. This is in contrast to the magnetotelluric vertical magnetic field responses (tippers), which are, to first order, sensitive to lateral conductivity variations in the vicinity of the observation site.

Finally, the best-fitting conductivity models were used to predict magnetic fields at considered locations. Fig. 17 compares observed and modelled field variations during a magnetically quiet period. Note that the modelled variations vary daily since they depend on the external source coefficients determined in Section 2.2. Generally larger mismatch for the X component can probably be attributed to its higher susceptibility to magnetospheric disturbances and polar current systems (Lühr *et al.* 2017).

6 CONCLUSIONS

In this study, we derived and extensively tested the concept of TFs that relate global expansion coefficients describing the source with a locally measured EM field. This methodology was applied to mantle

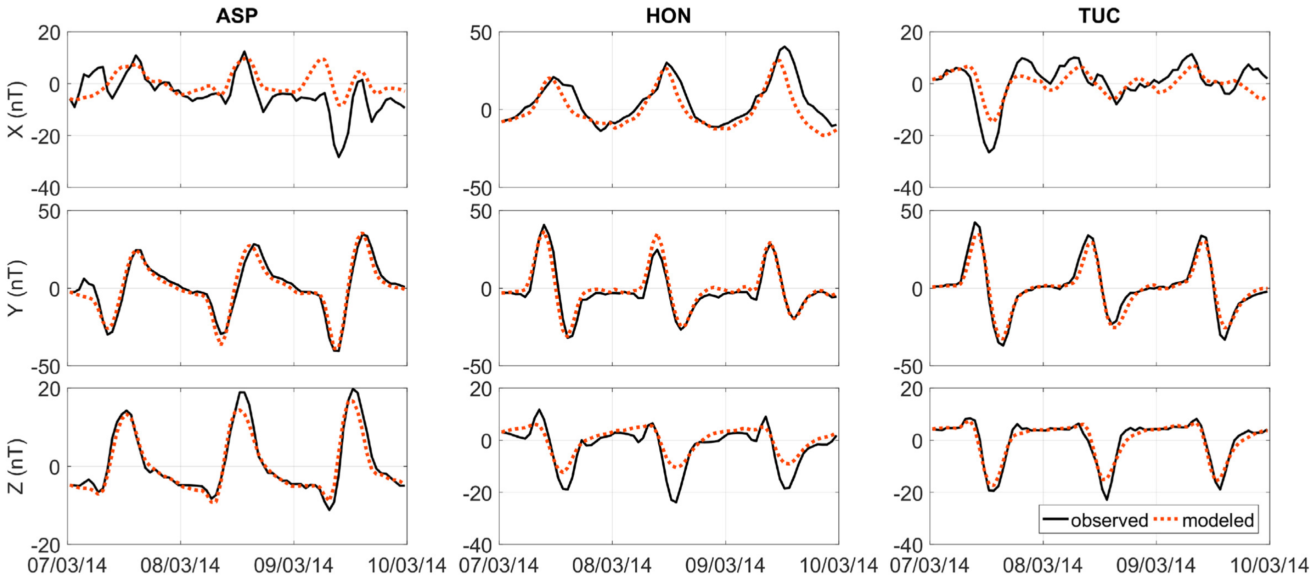

Figure 17. Observed and modelled magnetic variations during a magnetically quiet, equinoctial time period in March 2014. Modelled variations are obtained using the best-fitting conductivity models from Fig. 15.

conductivity sounding with daily variations of the magnetic field observed at the ground. We showed that responses at periods 4–24 hr enable probing Earth's electrical conductivity in the upper mantle and parts of the mantle transition zones, where both magnetotelluric and magnetospheric responses lack resolution.

Using a source parametrization in terms of SH functions and a prior 3-D conductivity model, which consisted of a global 1-D mantle overlaid by non-uniform continents and oceans of laterally variable (2-D) conductance, we estimated external source coefficients from the tangential magnetic field components measured at a global network of magnetic observatories. The reconstructed global source was then used to estimate local TFs using vertical magnetic field component, which is much more sensitive to the induced EM field compared to tangential components.

In contrast to the potential method, our approach can readily be applied to sea-bottom data, as well as electric field measurements. However, it requires making a prior assumption about the subsurface conductivity. The choice of the prior model affects the TFs, but we anticipate that repeating the source recovery several times with recovered local models will eventually lead to an equilibrium between them and minimize the potential bias.

In this study, the source parametrization consisted of a small set of SH functions tailored towards describing Sq variations. While this parametrization is suitable for describing source currents during magnetically quiet conditions and equinoctial months, it becomes less efficient during magnetically disturbed times. A possibly more advantageous approach is to use spatial modes derived from physics-based ionospheric and magnetospheric models. The potential of this approach should be explored in future works.

Finally, we performed 1-D inversions of the estimated TFs at a few locations. Inversions at the coastal and island locations invoked 3-D forward operator to account for the ocean induction effect. The models exhibit significant lateral variability of the upper mantle conductivity matching the locally plausible geologic scenarios. Furthermore, none of the models appear to be biased by a prior model used to reconstruct the source geometry.

ACKNOWLEDGEMENTS

MG was supported by ETH Grant No. ETH-3215-2. The authors acknowledge British Geological Survey, World Data Center Geomagnetism (Edinburgh), INTERMAGNET and the many institutes around the world that operate magnetic observatories. We also want to thank two anonymous reviewers for their comments, which helped improve the manuscript significantly.

REFERENCES

Alekseev, D., Kuvshinov, A. & Palshin, N., 2015. Compilation of 3D global conductivity model of the Earth for space weather applications, *Earth, Planets Space,* **67**(1), 1–11.

Bahr, K. & Filloux, H.J., 1989. Local Sq response functions from EMSLAB data, *J. geophys. Res.: Solid Earth,* **94**(B10), 14 195–14 200.

Bailey, R., 1969. Inversion of the geomagnetic induction problem, *Proc. R. Soc. Lond.,* **315,** 185–194.

Banks, R., 1969. Geomagnetic variations and the electrical conductivity of the upper mantle, *Geophys. J. Int.,* **17**(5), 457–487.

Campbell, W., Barton, C. & Welsh, W., 1998. Quiet-day ionospheric currents and their application to upper mantle conductivity in Australia, *Earth, Planets Space,* **50**(4), 347–360.

Constable, S. & Heinson, G., 2004. Hawaiian hot-spot swell structure from seafloor MT sounding, *Tectonophysics,* **389**(1-2), 111–124.

Egbert, G.D. & Booker, J.R., 1992. Very long period magnetotellurics at Tucson observatory: implications for mantle conductivity, *J. geophys. Res.: Solid Earth,* **97**(B11), 15 099–15 112.

Egbert, G.D. & Erofeeva, S.Y., 2002. Efficient inverse modeling of barotropic ocean tides, *J. Atmos. Oceanic Technol.,* **19**(2), 183–204.

Fainberg, E., Kuvshinov, A., Mishina, L. & Singer, B., 1990. The new approach to global deep soundings, *Pure appl. Geophys.,* **134,** 527–531.

Fukao, Y., Koyama, T., Obayashi, M. & Utada, H., 2004. Trans-Pacific temperature field in the mantle transition region derived from seismic and electromagnetic tomography, *Earth planet. Sci. Lett.,* **217**(3), 425–434.

Grayver, A. & Kuvshinov, A., 2016. Exploring equivalence domain in non-linear inverse problems using Covariance Matrix Adaption Evolution Strategy (CMAES) and random sampling, *Geophys. J. Int.,* **205**(2), 971–987.

Grayver, A.V., Schnepf, N.R., Kuvshinov, A.V., Sabaka, T.J., Manoj, C. & Olsen, N., 2016. Satellite tidal magnetic signals constrain oceanic lithosphere-asthenosphere boundary, *Sci. Adv.,* **2**(9), e1600798.

Grayver, A.V., Munch, F.D., Kuvshinov, A.V., Khan, A., Sabaka, T.J. & Tøffner-Clausen, L., 2017. Joint inversion of satellite-detected tidal and magnetospheric signals constrains electrical conductivity and water content of the upper mantle and transition zone, *Geophys. Res. Lett.,* **44**(12), 6074–6081.

Guzavina, M., Grayver, A. & Kuvshinov, A., 2018. Do ocean tidal signals influence recovery of solar quiet variations? *Earth, Planets Space,* **70**(5), doi:10.1186/s40623-017-0769-1.

Haines, P., Hand, M. & Sandiford, M., 2001. Palaeozoic synorogenic sedimentation in central and northern Australia: a review of distribution and timing with implications for the evolution of intracontinental orogens, *Aust. J. Earth Sci.,* **48**(6), 911–928.

Hansen, N. & Ostermeier, A., 2001. Completely derandomized self-adaptation in evolution strategies, *Evolut. Comput.,* **9**(2), 159–195.

Hirth, G., Evans, R.L. & Chave, A.D., 2000. Comparison of continental and oceanic mantle electrical conductivity: is the Archean lithosphere dry? *Geochem. Geophys. Geosyst.,* **1**(12), doi:10.1029/2000GC000048.

ISGI, 2018. International Service of Geomagnetic Indices (ISGI), Available at: http://isgi.unistra.fr/indices_aa.php.

Jiracek, G., 1990. Near-surface and topographic distortions in electromagnetic induction, *Surv. Geophys.,* **11**(2-3), 163–203.

Karato, S.-i. & Wang, D., 2013. Electrical conductivity of minerals and rocks, in *Physics and Chemistry of the Deep Earth,* pp. 145–182, ed. Karato, S.-I., John Wiley & Sons, Ltd.

Katsura, T. & Yoshino, T., 2015. Heterogeneity of electrical conductivity in the oceanic upper mantle, in *The Earth's Heterogeneous Mantle,* pp. 173–204, Springer.

Kelbert, A., Egbert, G.D. & Schultz, A., 2008. Non-linear conjugate gradient inversion for global EM induction: resolution studies, *Geophys. J. Int.,* **173**(2), 365–381.

Kelbert, A., Schultz, A. & Egbert, G., 2009. Global electromagnetic induction constraints on transition-zone water content variations, *Nature,* **460,** 1003–1007.

Koch, S. & Kuvshinov, A., 2013. Global 3-D EM inversion of Sq variations based on simultaneous source and conductivity determination: concept validation and resolution studies, *Geophys. J. Int.,* **195**(1), 98–116.

Koch, S. & Kuvshinov, A., 2015. 3-D EM inversion of ground based geomagnetic Sq data. Results from the analysis of Australian array (AWAGS) data, *Geophys. J. Int.,* **200**(3), 1284–1296.

Koyama, T., Shimizu, H., Utada, H., Ichiki, M., Ohtani, E. & Hae, R., 2006. *Water Content in the Mantle Transition Zone Beneath the North Pacific Derived from the Electrical Conductivity Anomaly,* pp. 171–179, American Geophysical Union (AGU).

Koyama, T., Khan, A. & Kuvshinov, A., 2014. Three-dimensional electrical conductivity structure beneath Australia from inversion of geomagnetic observatory data: evidence for lateral variations in transition-zone temperature, water content and melt, *Geophys. J. Int.,* **196,** 1330–1350.

Kuvshinov, A., 2008. 3-D global induction in the oceans and solid Earth: recent progress in modeling magnetic and electric fields from sources of magnetospheric, ionospheric and oceanic origin, *Surv. Geophys.,* **29**(2), 139–186.

Kuvshinov, A. & Semenov, A., 2012. Global 3-D imaging of mantle electrical conductivity based on inversion of observatory C-responses–I. An approach and its verification, *Geophys. J. Int.,* **189**(3), 1335–1352.

Lilley, F., Woods, D. & Sloane, M., 1981. Electrical conductivity profiles and implications for the absence or presence of partial melting beneath central and southeast Australia, *Phys. Earth planet. Inter.,* **25**(4), 419–428.

Lindzen, R. & Chapman, S., 1969. Atmospheric tides, *Space Sci. Rev.,* **10**(1), 3–188.

Lizarralde, D., Chave, A., Hirth, G. & Schultz, A., 1995. Northeastern Pacific mantle conductivity profile from long-period magnetotelluric sounding using Hawaii-to-California submarine cable data, *J. geophys. Res.: Solid Earth,* **100**(B9), 17 837–17 854.

Lühr, H., Xiong, C., Olsen, N. & Le, G., 2017. Near-earth magnetic field effects of large-scale magnetospheric currents, *Space Sci. Rev.,* **206,** 521–545.

Macmillan, S. & Olsen, N., 2013. Observatory data and the Swarm mission, *Earth, Planets Space,* **65**(11), 15.

Mayaud, P.N., 1980. *Derivation, Meaning, and Use of Geomagnetic Indices,* Vol. **22,** AGU Monography Series, Washington DC.

Neal, S.L., Mackie, R.L., Larsen, J.C. & Schultz, A., 2000. Variations in the electrical conductivity of the upper mantle beneath North America and the Pacific Ocean, *J. geophys. Res.: Solid Earth,* **105**(B4), 8229–8242.

Olsen, N., 1991. Untersuchung von tagesperiodischen Variationen des Erdmagnetfeldes mit neueren statistischen Methoden, *PhD thesis*, Georg-August-Universität zu Göttingen.

Olsen, N., 1992. Day-to-day C-response estimation for Sq from 1 cpd to 6 cpd using the Z:Y-method, *J. Geomag. Geoelectr.,* **44**(6), 433–447.

Olsen, N., 1998. The electrical conductivity of the mantle beneath Europe derived from C-responses from 3 to 720 hr, *Geophys. J. Int.,* **133**(2), 298–308.

Pankratov, O. & Kuvshinov, A., 2010. Fast calculation of the sensitivity matrix for responses to the Earth's conductivity: general strategy and examples, *Izvest., Phys. Solid Earth,* **46**(9), 788–804.

Parker, B.B., 2007. Tidal Analysis and Prediction. NOAA Special Publication NOS CO-OPS 3, Available at: https://tidesandcurrents.noaa.gov/publications/Tidal_Analysis_and_Predictions.pdf.

Parkinson, W.D., 1983. *Introduction to Geomagnetism,* Scottish Academic Press.

Püthe, C. & Kuvshinov, A., 2014. Mapping 3-D mantle electrical conductivity from space: a new 3-D inversion scheme based on analysis of matrix Q-responses, *Geophys. J. Int.,* **197,** 768–784.

Püthe, C., Kuvshinov, A., Khan, A. & Olsen, N., 2015a. A new model of Earth's radial conductivity structure derived from over 10 yr of satellite and observatory magnetic data, *Geophys. J. Int.,* **203**(3), 1864–1872.

Püthe, C., Kuvshinov, A. & Olsen, N., 2015b. Handling complex source structures in global EM induction studies: from C-responses to new arrays of transfer functions, *Geophys. J. Int.,* **201**(1), 318–328.

Sabaka, T.J., Hulot, G. & Olsen, N., 2010. Mathematical properties relevant to geomagnetic field modeling, in *Handbook of Geomathematics,* pp. 503–538, eds Freeden, W., Nashed, M.Z. & Sonar, T., Springer-Verlag.

Schmucker, U., 1970. Anomalies of geomagnetic variations in the southwestern United States, in *Bulletin of the Scripps Institution of Oceanography,* University of California.

Schmucker, U., 1984. Magnetic and electric fields due to electromagneic induction by external sources, in *Landolt-Börnstein: Numerical Data and Functional Relationships in Science and Technology,* Vol. 2: Geophysics of the Solid Earth, the Moon and the Planets. Subvolume b of New Series. Group V: Geophysics and Space Research, pp. 100–125, Springer-Verlag.

Schmucker, U., 1999. A spherical harmonic analysis of solar daily variations in the years 1964–1965: response estimates and source fields for global induction—I. Methods, *Geophys. J. Int.,* **136**(2), 439–454.

Semenov, A. & Kuvshinov, A., 2012. Global 3-D imaging of mantle conductivity based on inversion of observatory C-responses—II. Data analysis and results, *Geophys. J. Int.,* **191**(3), 965–992.

Shimizu, H., Utada, H., Baba, K., Koyama, T., Obayashi, M. & Fukao, Y., 2010. Three-dimensional imaging of electrical conductivity in the mantle transition zone beneath the North Pacific Ocean by a semi-global induction study, *Phys. Earth planet. Inter.,* **183**(1), 252–269, Special Issue on Deep Slab and Mantle Dynamics.

Simpson, F., 2002. A comparison of electromagnetic distortion and resolution of upper mantle conductivities beneath continental Europe and the Mediterranean using islands as windows, *Phys. Earth planet. Inter.,* **129**(1), 117–130.

Simpson, F., Steveling, E. & Leven, M., 2000. The effect of the Hawaiian plume on the magnetic daily variation, *Geophys. Res. Lett.,* **27**(12), 1775–1778.

Space Weather Canada, 2019. Solar radio flux, Avaliable at: http://www.spaceweather.gc.ca/solarflux/sx-5-en.php.

Srivastava, B.J., 1966. Theory of the magnetotelluric method of a spherical conductor, *Geophys. J. R. astr. Soc.,* **11,** 373–387.

Sun, J., Kelbert, A. & Egbert, G.D., 2015. Ionospheric current source modeling and global geomagnetic induction using ground geomagnetic observatory data, *J. geophys. Res.: Solid Earth,* **120**(10), 6771–6796.
Tarits, P. & Mandea, M., 2010. The heterogeneous electrical conductivity structure of the lower mantle, *Phys. Earth planet. Inter.,* **183**(1), 115–125.
Utada, H., Koyama, T., Obayashi, M. & Fukao, Y., 2009. A joint interpretation of electromagnetic and seismic tomography models suggests the mantle transition zone below Europe is dry, *Earth planet. Sci. Lett.,* **281**(3), 249–257.
Winch, D., 1981. Spherical harmonic analysis of geomagnetic tides, 1964-1965, *Phil. Trans. R. Soc. Lond., A, Math. Phys. Sci.,* **303**(1473), 1–104.
Yamazaki, Y. & Maute, A., 2017. Sq and EEJ—a review on the daily variation of the geomagnetic field caused by ionospheric dynamo currents, *Space Sci. Rev.,* **206,** 299–405.
Yamazaki, Y., Häusler, K. & Wild, J.A., 2016. Day-to-day variability of midlatitude ionospheric currents due to magnetospheric and lower atmospheric forcing, *J. geophys. Res.: Space Phys.,* **121**(7), 7067–7086.
Yoshino, T., 2010. Laboratory electrical conductivity measurement of mantle minerals, *Surv. Geophys.,* **31**(2), 163–206.
Yoshino, T., Matsuzaki, T., Yamashita, S. & Katsura, T., 2006. Hydrous olivine unable to account for conductivity anomaly at the top of the asthenosphere, *Nature,* **443**(7114), 973.

APPENDIX A: MAGNETIC FIELD ABOVE CONDUCTING EARTH

Above the Earth's surface and in the electrically insulating atmosphere, first equation in a system of eq. (1) reduces to $\nabla \times \vec{B} = 0$ due to vanishing conductivity and in the absence of source currents. $\vec{B}$ is thus a potential field and can be written as the gradient of a scalar magnetic potential V, that is

$$\vec{B} = -\nabla V. \tag{A1}$$

Since $\vec{B}$ is solenoidal (i.e. $\nabla \cdot \vec{B} = 0$), V satisfies Laplace's equation,

$$\nabla^2 V = 0. \tag{A2}$$

The solution of the Laplace's equation in spherical geometry can be represented as a sum of external (inducing) and internal (induced) parts

$$V = V^{ext} + V^{int}, \tag{A3}$$

with

$$V^{ext}(\vec{r}, \omega) = a \sum_{n,m} \varepsilon_n^m(\omega) \left(\frac{r}{a}\right)^n S_n^m(\vartheta, \varphi), \tag{A4}$$

$$V^{int}(\vec{r}, \omega) = a \sum_{k,l} \iota_k^l(\omega) \left(\frac{a}{r}\right)^{(k+1)} S_k^l(\vartheta, \varphi). \tag{A5}$$

Here, $\varepsilon_n^m(\omega)$ and $\iota_k^l(\omega)$ are the spherical harmonic expansion (SHE) coefficients of the external and internal parts of the potential, respectively. Using eqs (A1) and (A3)–(A5), we can write the magnetic field above the Earth as follows:

$$\vec{B} = \vec{B}^{ext} + \vec{B}^{int}, \tag{A6}$$

or in the component form

$$B_r = -\sum_{n,m} n\varepsilon_n^m(\omega) \left(\frac{r}{a}\right)^{n-1} S_n^m(\vartheta, \varphi) + \sum_{k,l} (k+1)\iota_k^l(\omega) \left(\frac{a}{r}\right)^{k+2} S_k^l(\vartheta, \varphi), \tag{A7}$$

$$\vec{B}_\tau = -\sum_{n,m} \varepsilon_n^m(\omega) \left(\frac{r}{a}\right)^{n-1} \nabla_\perp S_n^m(\vartheta, \varphi) - \sum_{k,l} \iota_k^l(\omega) \left(\frac{a}{r}\right)^{k+2} \nabla_\perp S_k^l(\vartheta, \varphi). \tag{A8}$$

Note that we deliberately separate summation in eqs (A4)–(A5) and (A7)–(A8) into two parts and explain the reasoning for this in Appendix E.

APPENDIX B: SOURCE PARAMETRIZATION

Daily variations of the geomagnetic field originate mostly from a double-vortex Sq electric current system, in which electric currents flow counter-clockwise in the Northern Hemisphere and clockwise in the Southern Hemisphere. Recall that the produced Sq variations at the ground are periodic, and the majority of the signal is contained in the first six 24-hr harmonics $p = 1, 2, ..., 6$ at frequencies $\omega_p = \frac{2\pi p}{T}$ where $T = 24$ hr.

Analysis of ground Sq variations does not yield a unique underlying current system (Yamazaki *et al.* 2016). However, by adopting the *equivalent current system* concept, it is possible to determine this (2-D) system from the SH analysis of ground Sq variations. In this paper, we adopted SH representation of the Sq current system by Schmucker (1999). His selection of SH is briefly sketched in the following.

Sq vortexes are predominantly a local-time phenomenon, that is they follow the westward movement of the Sun with respect to an observer on Earth. The local-time dependency is governed by $m = p$. According to Schmucker (1999), four local-time terms at each p are indispensable. The principal (dominant) term is the equator-antisymmetric SH, S_{p+1}^p, which describes two vortexes in local time (one sign change with respect to the equator follows from $n - |m|$). Due to the structure of atmospheric tides (e.g. Lindzen & Chapman 1969), the dominant term is coupled with another equator-antisymmetric SH, S_{p+3}^p (Winch 1981, p. 34), which causes compression of the vortexes towards the vortex foci. Furthermore, two equator-symmetric terms, S_p^p and S_{p+2}^p, govern the hemispherical asymmetry during summer and winter months (in our study these terms have tiny magnitudes since we work with equinoctial months).

Additionally, some part of variations does not occur in local time. The number of non local-time terms ($m \neq p$), also termed general terms, has to be chosen such that the least-squares (LS) fit of SH terms to the measured Sq variations is both close and stable. Schmucker uses the following expression to define the total number of SH terms, M, at each p

$$M = K(1 + 2L), \tag{B1}$$

where K and L control the number of local-time and general terms, respectively. Following Schmucker, $M = 12$ yields a good balance between the stability and closeness of LS fit. Accordingly, $K = 4$ and $L = 1$, that is four local-time and eight general terms at each p are used.

The selection of these twelve terms at each p is controlled by the double sum given in Appendix B in Schmucker (1999), and reproduced in eq. (12). Note that in this equation the standard order of summation over n first and m second is reversed. The obtained (n, m) combinations are listed in Table 1. Note that at $p = 1$, combination $n = 0$, $m = 0$ is forbidden since $\nabla \cdot \vec{B} = 0$ should be satisfied everywhere (Sabaka *et al.* 2010). Hence, eq. (12) gives 11 SHs for $p = 1$ and 12 SHs for $p = 2, \ldots, 6$.

APPENDIX C: SENSITIVITY OF MAGNETIC FIELD COMPONENTS TO CONDUCTIVITY STRUCTURE

To demonstrate that tangential magnetic field components are indeed less sensitive to the conductivity structures than the vertical component, we computed magnetic field in 1-D and 3-D models of the Earth. 1-D model was taken from Grayver *et al.* (2017). 3-D model comprises the same 1-D conductivity model but overlain by a thin shell of known laterally variable (2-D) conductance. For both cases, the results correspond to Sq variations of 16 March 2011.

Fig. C1 presents real parts of magnetic fields at the period of 24 hr. As expected, X and Y components from 1-D model (depicted on the left) are larger in magnitude than Z. In fact, X and Ycomponents reach up to 25 and 15 nT, respectively, while Z component reaches at most 5 nT. However, the differences between the fields from 1-D and 3-D models (depicted on the right) are significantly larger for Z relative to X and Y. For instance, at some locations such as northern and southern edges of Southern America the differences for Z component exceed 100 per cent. Note that larger differences in Z than X and Y are also observed for imaginary parts and other periods of Sq variations.

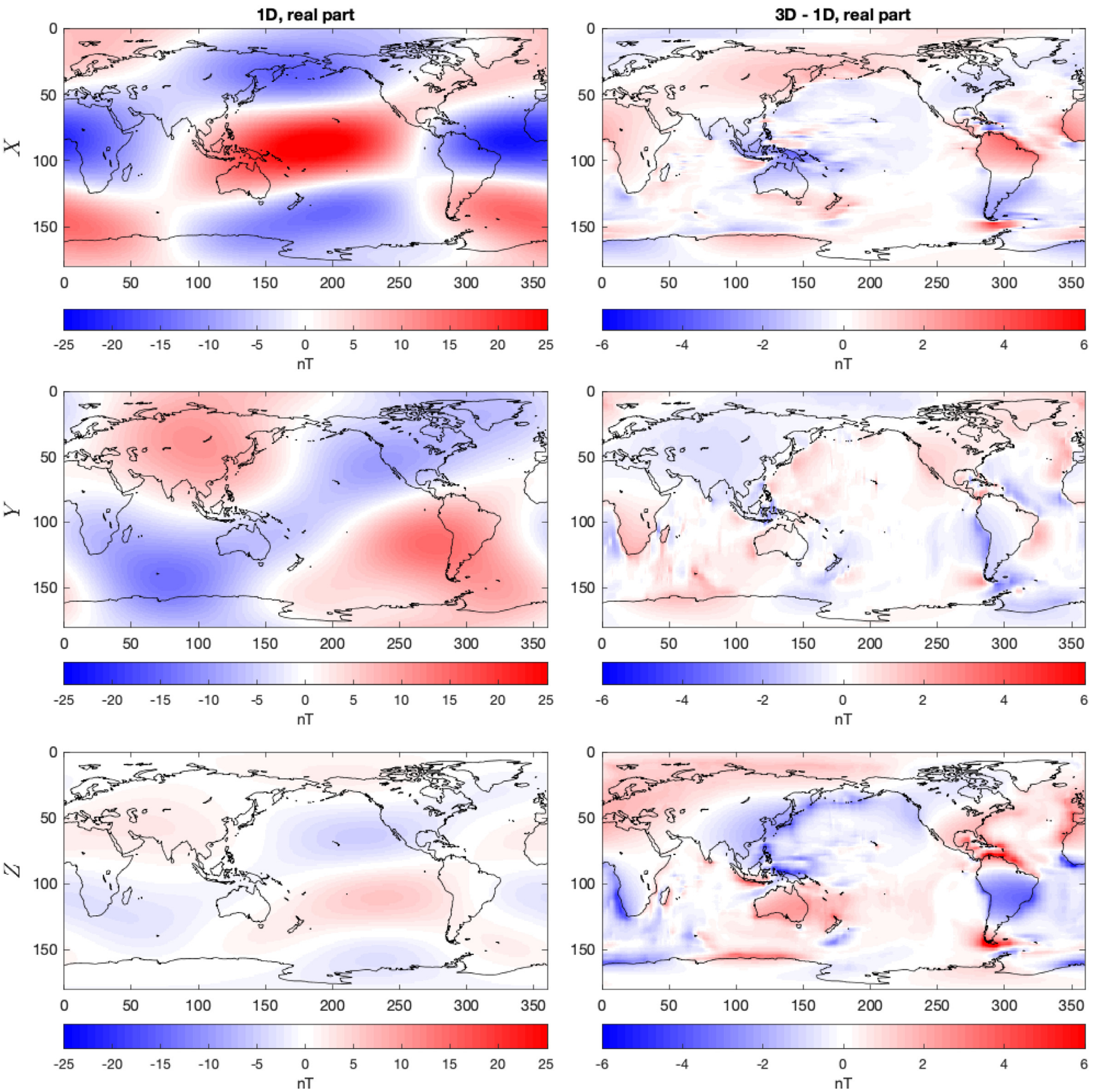

Figure C1. Real parts of Sq magnetic field components at the period of 24 hr. Left: results from 1-D modelling. Right: differences between results from 3-D and 1-D modelling (see text of this Appendix for more explanation).

APPENDIX D: CODES, NAMES AND COORDINATES OF OBSERVATORIES USED IN THE STUDY

Table D1. Geomagnetic observatories acronyms, names, geocentric (GC), geomagnetic (GM) and quasi dipole (QD) coordinates for IGRF-12 epoch 2015.

Code	Station	ϑ^{GC}	φ^{GC}	ϑ^{GM}	φ^{GM}	ϑ^{QD}	φ^{QD}
AAA	Alma Ata	43.06	76.92	34.59	153.27	39.04	150.11
ABG	Alibag	18.52	72.87	10.51	146.89	12.53	146.02
AIA	Argentine Islands	−65.10	295.75	−55.55	6.23	−50.89	9.60
AMS	Amsterdam Island	−37.61	77.57	−45.78	145.63	−48.85	140.45
AMT	Amatsia	31.38	34.92	28.05	112.72	25.64	107.73
API	Apia	−13.71	188.22	−15.04	263.30	−15.66	−96.48
AQU	L'Aquila	42.19	13.32	42.14	94.70	36.50	87.89
ARS	Arti	56.26	58.57	49.34	140.10	52.76	132.24
ASC	Ascension Island	−7.90	345.62	−2.77	57.48	−20.03	56.08
ASP	Alice Springs	−23.63	133.88	−32.16	208.89	−33.57	−152.00
BDV	Budkov	48.89	14.02	48.53	97.65	44.33	89.42
BEL	Belsk	51.65	20.80	50.08	105.16	47.50	95.91
BFE	Brorfelde	55.45	11.67	55.23	98.29	51.83	88.94
BFO	Black Forest	48.14	8.32	48.75	91.83	43.47	84.36
BGY	Bar Gyora	31.55	35.08	28.19	112.91	25.84	107.89
BMT	Beijing Ming Tombs	40.11	116.20	30.58	187.84	35.04	−169.84
BNG	Bangui	4.30	18.57	4.04	91.90	−7.32	93.25
BOU	Boulder	39.94	254.77	47.82	322.03	48.35	−38.20
BOX	Borok	57.89	38.22	53.46	123.45	54.32	113.09
BSL	Stennis Space Center	30.18	270.37	39.34	340.92	40.54	−17.58
CBI	Chichijima	26.94	142.18	18.92	212.55	19.84	−145.40
CDP	Chengdu	30.83	103.70	21.22	176.62	25.61	176.97
CKI	Cocos-Keeling Islands	−12.10	96.83	−21.56	168.92	−21.87	169.00
CLF	Chambon la Foret	47.83	2.27	49.46	85.72	43.20	79.17
CNB	Canberra	−35.13	149.37	−42.00	227.41	−45.02	−132.38
CNH	Changchun	43.64	125.30	34.42	195.67	38.16	−160.64
COI	Coimbra	40.03	351.58	43.62	72.24	34.06	68.89
CTA	Charters Towers	−19.96	146.27	−27.32	221.63	−28.89	−138.77
CTS	Castello Tesino	45.86	11.65	45.98	94.26	40.78	86.87
CYG	Cheongyang	36.18	126.85	27.05	197.59	30.25	−159.47
CZT	Port Alfred	−46.24	51.87	−51.04	114.96	−53.21	107.76
DLR	Del Rio	29.32	259.08	37.68	328.53	38.27	−31.86
DLT	Dalat	11.84	108.42	2.21	181.03	5.17	−178.92
DOU	Dourbes	49.91	4.60	51.08	88.87	45.62	81.56
EBR	Ebro	40.77	0.33	42.91	81.40	34.67	76.44
ELT	Eilat	29.50	34.95	26.20	112.37	23.54	107.82
ESA	Esashi	39.05	141.35	30.89	210.38	32.34	−145.75
ESK	Eskdalemuir	55.14	356.80	57.41	83.52	52.14	76.51
EYR	Eyrewell	−43.21	172.40	−46.59	254.05	−49.88	−102.78
FRD	Fredericksburg	38.03	282.63	47.62	354.46	47.89	−0.30
FRN	Fresno	36.90	240.28	43.08	306.69	42.63	−54.44
FUQ	Fuquene	5.43	286.27	15.06	358.86	16.18	0.72
FUR	Furstenfeldbruck	47.98	11.28	48.10	94.66	43.26	86.88
GAN	Gan	−0.69	73.15	−8.64	145.33	−8.84	145.61
GCK	Grocka	44.44	20.77	43.10	102.56	39.37	94.78
GLM	Golmud	36.22	94.90	26.79	168.75	31.48	168.24
GNA	Gnangara	−31.61	115.95	−41.12	189.71	−43.18	−172.00
GNG	Gingin	−31.18	115.72	−40.69	189.43	−42.70	−172.24
GUA	Guam	13.50	144.87	5.80	216.51	6.13	−143.01
GUI	Guimar-Tenerife	28.16	343.57	33.18	61.09	19.70	60.41
GZH	Zhaoqing	22.83	112.45	13.23	184.81	16.95	−174.60

Table D1. Continued

Code	Station	ϑ^{GC}	φ^{GC}	ϑ^{GM}	φ^{GM}	ϑ^{QD}	φ^{QD}
HAD	Hartland	50.81	355.52	53.47	80.11	47.11	74.22
HBK	Hartebeesthoek	−25.73	27.70	−27.07	95.58	−36.32	97.01
HER	Hermanus	−34.24	19.23	−34.00	85.32	−42.85	84.61
HLP	Hel	54.42	18.82	53.07	104.51	50.57	94.80
HON	Honolulu	21.19	202.00	21.65	270.85	21.03	−89.08
HRB	Hurbanovo	47.67	18.18	46.66	101.18	42.99	92.88
HTY	Hatizyo	32.94	139.80	24.68	209.69	26.08	−147.37
HYB	Hyderabad	17.31	78.55	8.82	152.24	10.96	151.66
IPM	Easter Island	−27.01	250.58	−19.17	325.61	−19.68	−32.37
IRT	Irkutsk	51.98	104.45	42.36	177.57	47.93	178.52
IZN	Iznik	40.31	29.73	37.63	109.87	35.18	102.79
JAI	Jaipur	26.71	75.82	18.41	150.48	21.42	148.98
KAK	Kakioka	36.05	140.18	27.81	209.69	29.28	−146.90
KDU	Kakadu	−12.60	132.47	−21.28	206.37	−21.48	−154.35
KEP	King Edward Point	−54.10	323.50	−46.01	29.85	−45.30	25.62
KHB	Khabarovsk	47.42	134.68	38.72	203.44	41.48	−151.73
KIV	Kiev	50.53	30.30	47.50	113.50	46.44	104.31
KMH	Keetmanshoop	−26.38	18.12	−26.10	85.99	−37.16	87.06
KNY	Kanoya	31.25	130.88	22.35	201.64	24.83	−155.86
KNZ	Kanozan	35.07	139.95	26.81	209.59	28.27	−147.15
KOU	Kourou	5.18	307.28	14.22	20.48	7.71	22.43
KSH	Kashi	39.31	76.00	30.94	151.99	35.06	149.16
LIV	Livingston Island	−62.51	299.60	−53.05	9.36	−48.70	11.22
LMM	Maputo	−25.77	32.58	−27.91	100.45	−36.07	101.73
LNP	Lunping	24.85	121.17	15.48	192.98	18.78	−165.79
LON	Lonjsko Polje	45.21	16.67	44.52	98.89	40.12	91.19
LRM	Learmonth	−22.08	114.10	−31.64	187.33	−32.39	−173.52
LVV	Lviv	49.71	23.75	47.73	107.16	45.39	98.19
LZH	Lanzhou	35.90	103.85	26.29	176.82	31.04	177.35
MAB	Manhay	50.11	5.68	51.10	90.03	45.83	82.52
MGD	Magadan	59.95	151.02	52.45	214.55	54.22	−138.99
MIZ	Mizusawa	38.93	141.20	30.76	210.26	32.22	−145.89
MMB	Memambetsu	43.72	144.18	35.78	212.26	37.11	−143.19
MNK	Minsk	54.32	27.88	51.54	112.78	50.49	102.82
MOS	Moscow	55.29	37.32	51.07	121.58	51.61	111.69
MZL	Manzhouli	49.41	117.40	39.90	188.49	44.68	−168.34
NCK	Nagycenk	47.44	16.72	46.68	99.70	42.69	91.55
NEW	Newport	48.08	242.88	54.42	306.42	54.37	−54.11
NGK	Niemegk	51.88	12.68	51.63	97.58	47.76	88.87
NGP	Nagpur	21.00	79.03	12.47	153.01	15.03	152.17
NMP	Nampula	−15.00	39.25	−18.39	109.17	−25.25	111.33
NVS	Novosibirsk	54.67	83.23	45.73	160.20	51.08	156.81
ORC	Orcadas	−60.57	315.22	−51.81	21.79	−48.65	20.38
OTT	Ottawa	45.21	284.45	54.82	356.43	54.61	2.79
PAG	Panagjurishte	42.33	24.18	40.48	105.17	37.12	97.71
PEG	Pedeli	37.90	23.93	36.19	103.74	32.05	97.25
PET	Paratunka	52.78	158.25	46.16	222.65	46.56	−131.96
PHU	Phuthuy	20.91	105.97	11.28	178.66	14.93	178.86
PIL	Pilar	−31.50	296.12	−21.97	8.04	−20.31	5.81
PPT	Pamatai	−17.46	210.43	−15.05	285.79	−16.38	−73.70
PST	Port Stanley	−51.51	302.10	−42.15	12.32	−39.19	10.89
QGZ	Qiongzhong	18.88	109.80	9.26	182.33	12.77	−177.40
QIX	Qianling	34.37	108.20	24.74	180.75	29.31	−178.29

Table D1. Continued

Code	Station	ϑ^{GC}	φ^{GC}	ϑ^{GM}	φ^{GM}	ϑ^{QD}	φ^{QD}
QSB	Qsaybeh	33.69	35.65	30.21	113.90	28.27	108.40
QZH	Quanzhou	24.75	118.60	15.30	190.56	18.79	−168.35
SBL	Sable Island	43.74	299.98	53.09	15.23	49.83	22.77
SFS	San Fernando	36.28	353.80	39.60	73.50	29.26	70.32
SHL	Shillong	25.42	91.87	16.11	165.45	19.71	164.95
SHU	Shumagin	55.17	199.53	54.38	258.51	53.07	−99.27
SIL	Silchar	24.79	92.82	15.45	166.31	19.02	165.88
SJG	San Juan	18.00	293.85	27.57	6.95	26.06	11.59
SPT	San Pablo-Toledo	39.36	355.65	42.31	76.23	33.04	72.26
SSH	Sheshan	30.93	121.18	21.56	192.72	25.14	−165.39
STJ	St John’s	47.41	307.32	56.33	24.61	51.71	31.44
SUA	Surlari	44.49	26.25	42.26	107.76	39.66	99.80
TAM	Tamanrasset	22.66	5.53	24.30	82.30	12.70	80.30
TAN	Antananarivo	−18.80	47.55	−23.41	116.91	−28.40	118.07
TDC	Tristan da Cunha	−36.88	347.68	−31.70	54.76	−41.03	49.77
TEO	Teoloyucan	19.63	260.82	28.17	331.47	28.65	−29.12
TFS	Tblisi	41.91	44.70	36.97	124.16	37.73	117.44
THJ	Tonghai	23.86	102.70	14.26	175.59	18.09	175.70
THY	Tihany	46.71	17.90	45.77	100.58	41.87	92.49
TND	Tondano	1.28	124.95	−7.90	197.75	−6.34	−162.59
TRW	Trelew	−43.07	294.62	−33.51	6.35	−30.59	5.17
TSU	Tsumeb	−19.08	17.58	−18.84	86.90	−31.14	89.07
TUC	Tucson	31.99	249.27	39.35	317.41	39.30	−43.58
UJJ	Ujjain	23.04	75.78	14.76	150.10	17.39	148.94
VAL	Valentia	51.75	349.75	55.31	74.55	48.67	69.74
VIC	Victoria	48.33	236.58	53.78	299.33	53.38	−61.35
VSK	Visakhapatnam	17.62	83.33	8.79	156.87	11.17	156.41
VSS	Vassouras	−22.27	316.35	−13.78	27.49	−20.33	22.41
WHN	Wuhan	30.36	114.57	20.80	186.64	24.87	−172.06
WIC	Conrad Observatory	47.74	15.87	47.11	99.00	43.02	90.84
WIK	Wien Kobenzl	48.08	16.32	47.36	99.55	43.41	91.29
WNG	Wingst	53.57	9.07	53.86	94.87	49.75	86.21

APPENDIX E: Q-RESPONSE CONCEPT

E1 A case of 1-D Earth's model

If the conductivity of the Earth depends only on radius, r, i.e,

$$\sigma \equiv \sigma(r), \tag{E1}$$

then each external coefficient induces only one internal coefficient (of the same degree n and order m); their ratio (the so-called Q-response) is independent of m (e.g. Bailey 1969)

$$\iota_n^m(\omega) = Q_n(\omega)\varepsilon_n^m(\omega) \tag{E2}$$

and can be calculated using an appropriate recurrence formula. Based on Srivastava (1966) formalism, Parkinson (1983) presents such formula for the layered spherical Earth's model with a piece-wise constant conductivity distribution. Kuvshinov & Semenov (2012) present the recursion for the layered spherical Earth's model where conductivity distribution within the layer obeys the power law. Table E1 exemplifies the Q_n values for the global 1-D conductivity model obtained by Grayver *et al.* (2017).

From eqs (A7)–(A8) and (E2), it follows that at the surface of a 1-D Earth the magnetic field can be written as

$$B_r(r = a, \vartheta, \varphi, \omega) = -\sum_{n,m} \varepsilon_n^m(\omega)\,[n - (n+1)Q_n(\omega)]\, S_n^m(\vartheta, \varphi), \tag{E3}$$

$$\vec{B}_\tau(r = a, \vartheta, \varphi, \omega) = -\sum_{n,m} \varepsilon_n^m(\omega)\,[1 + Q_n(\omega)]\, \nabla_\perp S_n^m(\vartheta, \varphi). \tag{E4}$$

E2 A case of 3-D Earth's model

In a 3-D Earth, every external coefficient ε_n^m induces a whole series of internal coefficients ι_k^l, such that we can write

$$\iota_k^l(\omega) = \sum_{n,m} Q_{kn}^{lm}(\omega)\varepsilon_n^m(\omega), \tag{E5}$$

where Q_{kn}^{lm} forms a 2-D array of TFs which is referred to as a 'matrix Q-response' or a 'Q-matrix' (Püthe & Kuvshinov 2014). The diagonal elements of this matrix mostly describe the bulk conductivity and the stratification of the subsurface—in the case of a layered (1-D) Earth, they are equivalent to the scalar Q-responses. The off-diagonal elements describe a transfer of energy to coefficients of different degree and order, which only occurs if the subsurface has a 3-D structure.

Table E1. Real and imaginary parts of Q_n at periods of Sq variations for 1-D conductivity model by Grayver *et al.* (2017). The model is overlain by a surface thin shell of uniform conductance of 400 S. The latter value mimics averaged inland conductance.

Period	n	Re	Im
24.0	2	0.4373	0.0732
12.0	3	0.4614	0.0990
8.0	4	0.4591	0.1158
6.0	5	0.4452	0.1276
4.8	6	0.4261	0.1365
4.0	7	0.4048	0.1432

APPENDIX F: MODELLING TIDAL MAGNETIC SIGNALS

Ocean tides consist of a number of periodic tidal constituents caused by the gravitational forces between Earth, Sun and Moon (Parker 2007). Among large number of tidal constituents, several solar and lunar diurnal and semi-diurnal constituents dominate. Table F1 lists constituents (with the largest magnitudes) considered in this work. Bearing this information in mind, the tidal magnetic field can be written in time domain as

$$\vec{B}^{\text{tides}}(\vec{r}, t) = \mathrm{Re}\left[\sum_{k=1}^{8} f_k\, \vec{B}^{\text{tides}}(\vec{r}, \omega_k)\exp\left\{\mathrm{i}\left(\omega_k(t - t_0) + V_{0,k}(t_0) + u_k\right)\right\}\right]. \tag{F1}$$

Here, k stands for kth tidal constituent, ω_k is corresponding angular frequency, $V_{0,k}$ astronomical argument, t_0 reference time on 1 January 1992 at 00:00:00, u_k and f_k phase and amplitude modulating factors, respectively (Egbert & Erofeeva 2002). $\vec{B}^{\text{tides}}(\vec{r}, \omega_k)$ are numerical solutions of Maxwell's eq. (1) for a prior 3-D conductivity model and for an excitation by a corresponding extraneous current, $\vec{j}^{\text{tides}}$, which is confined to the oceans and is given by

$$\vec{j}^{\text{tides}}(\vartheta, \varphi, \omega_k) = \sigma_s(\vartheta, \varphi)\left(\vec{v}(\vartheta, \varphi, \omega_k) \times \vec{B}^{\text{main}}(\vartheta, \varphi)\right), \tag{F2}$$

where σ_s is conductivity of sea water, $\vec{B}^{\text{main}}$ is the Earth's main (core) magnetic field, $\vec{v} = \vec{u}/d$ with d being the height of the water column, and $\vec{u}(\vartheta, \varphi, \omega_k)$ is depth-integrated seawater velocity due to the kth tidal constituent. See Grayver *et al.* (2016) for more details about individual terms in eq. (F2).

Table F1. Principal tidal constituents and their periods (Parker 2007).

Constituent	Name	Period
Semi-diurnal		
Lunisolar	K2	11 hr 58 min
Principal solar	S2	12 hr
Principal lunar	M2	12 hr 25 min
Elliptical to M2	N2	12 hr 39 min
Diurnal		
Lunisolar	K1	23 hr 56 min
Principal solar	P1	24 hr 4 min
Principal lunar	O1	25 hr 49 min
Elliptical to O1	Q1	26 hr 52 min